UDC 551.501.71:519.281.2:551.524.77'47.5:551.507.362.2:535.853:551.521.32

A REGRESSION METHOD FOR OBTAINING REAL-TIME TEMPERATURE AND GEOPOTENTIAL HEIGHT PROFILES FROM SATELLITE SPECTROMETER MEASUREMENTS AND ITS APPLICATION TO NIMBUS 3 "SIRS" OBSERVATIONS

W. L. SMITH, H. M. WOOLF, and W. J. JACOB
Environmental Science Services Administration, Washington, D.C.

ABSTRACT

A least squares regression method is formulated for obtaining global temperature and geopotential height profiles from satellite radiation measurements, particularly those obtained by the Satellite Infra-Red Spectrometer (SIRS) aboard the Nimbus 3 satellite launched Apr. 14, 1969. Regression equations relating temperature and geopotential height to spectral radiance observations are derived. A method accounting for the influence of clouds, mountains, and hot terrain on the solutions is described. Results obtained from Nimbus 3 radiance data are presented.

The procedure described herein has been successfully applied to Nimbus 3 SIRS observations on a real-time basis. The temperature and geopotential heights obtained are being used operationally by the National Meteorological Center in their objective constant pressure analyses. Numerous meteorological results are given to demonstrate the usefulness of this new sounding tool.

1. INTRODUCTION

Recent studies on the temperature inversion problem by Wark and Fleming (1966), Rodgers (1966), Westwater and Strand (1968), and others indicate that maximum information about the atmosphere's thermal structure may be derived from satellite radiation observations through the use of statistical relationships. The advantages of such relationships are 1) they inherently contain the structure information necessary to recover detailed temperature profiles from relatively few thermal radiative measurements and 2) when derived from actual data (as in the procedure given here), the solutions are statistically optimum and computationally stable with respect to the physical and instrumental limitations that are encountered in practice (for example, clouds and measurement errors).

Investigations by Obukhov (1960) and Holmström (1963) concerning the statistical nature of the pressure-height distribution, the basic parameter used for weather prediction, suggest that the geopotential height distribution can be specified to a high degree of accuracy with relatively few statistical functions. (These investigators considered the specification with empirical orthogonal functions.) When using their concepts here, it is shown that the geopotential height profile as well as the temperature profile can be expressed directly in terms of spectral radiance observations. The expressions allow useful estimates of the pressure-height distribution to be obtained without prior knowledge of surface pressure, the parameter necessary for computing the geopotential height profile hydrostatically from the temperature profile. If the surface pressure or height of any pressure level is known, this information can be utilized with the statistical expressions to yield an improved estimate of the pressure-height profile.

From the above considerations, a regression model for deriving the atmosphere's temperature and geopotential height distribution from satellite radiation measurements was developed. Methods of accounting for the influences of clouds, high terrain, and hot terrain on the solutions have been devised. Results obtained from the application of this method in real time to radiance observations obtained by the SIRS aboard the Nimbus 3 satellite are presented.

2. SATELLITE OBSERVATIONS AND THEIR CORRELATION WITH ATMOSPHERIC TEMPERATURE AND GEOPOTENTIAL HEIGHT

The satellite observations used to calculate temperature and geopotential height profiles are obtained by the SIRS experiment aboard the Nimbus 3 spacecraft. This experiment is discussed by Wark and Hilleary (1969). Briefly, the SIRS measures the radiance leaving the earth-atmosphere system in seven narrow (5 cm^{-1}) spectral intervals of the 15-μm CO_2 band and one narrow (5 cm^{-1}) spectral interval of the 11-μm window region. The linear spatial resolution is about 225 km. The absolute accuracy of the earth-atmospheric radiance measurements is within $\pm$ 2 ergs $(sec\ cm^2\ sr\ cm^{-1})^{-1}$ (that is, within a few percent), and the relative accuracy and precision are better than $\pm$ 0.25 erg $(sec\ cm^2\ sr\ cm^{-1})^{-1}$ (within one-half of 1 percent). The SIRS experiment as superbly designed by Wark and Hilleary of the National Environmental Satellite Center provides the highly accurate measurements needed to determine the temperature and geopotential height distribution of the atmosphere.

Figure 1 illustrates the transmission of the atmosphere above atmospheric pressure levels for radiation in the eight SIRS channels (that is, spectral intervals of observa-

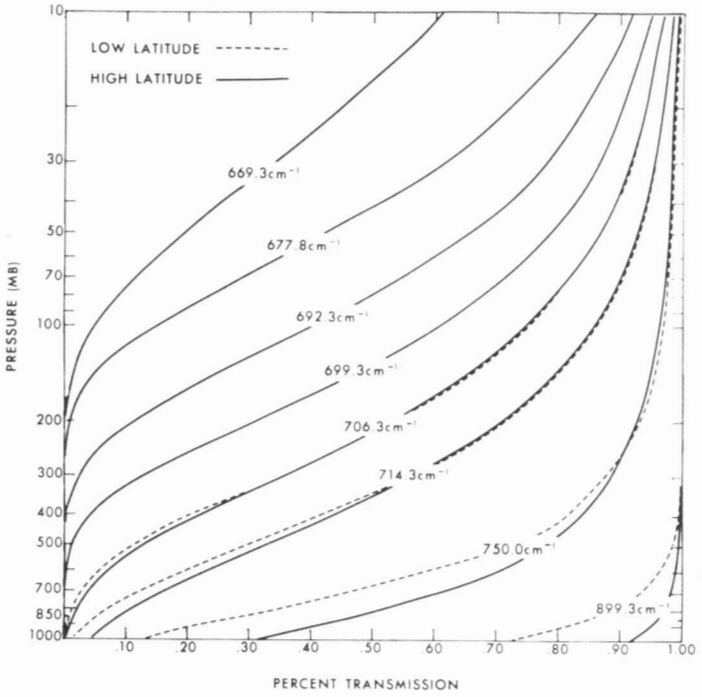

FIGURE 1.—Atmospheric transmission functions pertaining to the SIRS spectral intervals of observation for two different atmospheres.

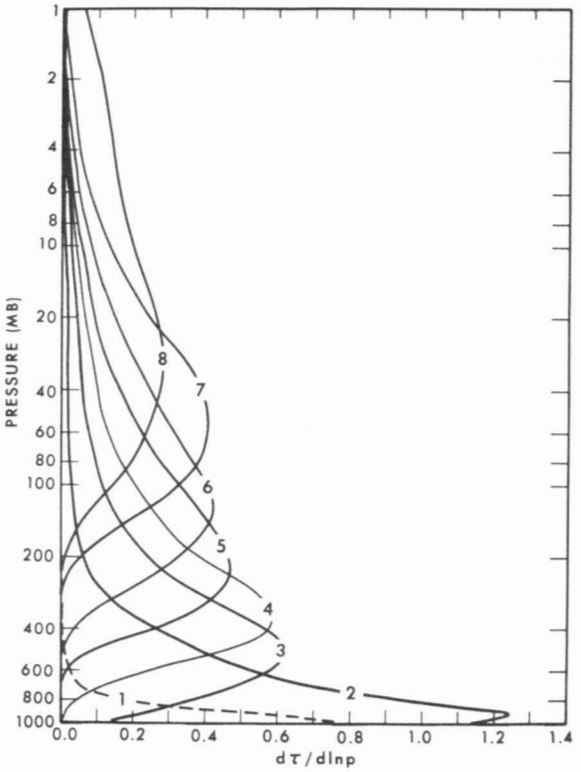

FIGURE 2.—Derivative of transmittance with respect to the logarithm of pressure. These functions approximately describe the relative sensitivity of the eight SIRS radiance observations to temperature variations in various altitude layers of the atmosphere.

tion) for a high- and low-latitude atmospheric situation. The differences in the transmission functions in the lowest atmospheric levels result mainly from water vapor differences in the two atmospheric situations while the smaller differences at higher levels result from temperature discrepancies. The water vapor and temperature dependence of the transmissions is considered here only for the four most transparent spectral channels.

Figure 2 shows derivatives of the transmission functions for a "standard atmosphere" with respect to the logarithm of pressure. These derivative functions are the Planck radiance "weighting" functions of the radiative transfer equation. As such, they illustrate the layers of the atmosphere most vividly sensed by the various SIRS spectral channels. As may be seen from figure 2, various atmospheric layers below the 10-mb level are selectively observed by the SIRS.

Table 1 shows typical correlations of the radiances measured in the seven 15-μm CO_2 spectral intervals for clear-sky conditions, with the temperature measured at various pressure levels by radiosondes between 35° N. and 55° N. The samples consisted of 700 sets of observations. The different correlations of the measured energies with the temperatures of various atmospheric levels is clearly illustrated in table 1. The levels of maximum positive correlations are in general agreement with the theoretical weighting functions given in figure 2. The relatively low correlations observed at 30 and 10 mb are partially a result of radiosonde errors at these levels.

TABLE 1.—*Radiance-temperature correlation matrix for (A) May–June 1969 and (B) October–November 1969*

Pressure level (mb)		Channel (central wave number in cm⁻¹)						
		669.3	677.8	692.3	699.3	706.3	714.3	750.0
A	1,000	−0.69	−0.70	−0.74	−0.73	0.35	0.74	0.91
	850	−.73	−.79	−.82	−.78	.50	.86	.91
	700	−.80	−.86	−.90	−.83	.64	.93	.89
	500	−.81	−.87	−.91	−.81	.72	.92	.78
	400	−.78	−.85	−.89	−.77	.73	.88	.70
	300	−.74	−.81	−.82	−.66	.76	.82	.60
	250	−.44	−.48	−.39	−.15	.63	.42	.18
	200	.62	.67	.80	.87	−.33	−.71	−.71
	150	.75	.82	.90	.85	−.55	−.82	−.74
	100	.88	.94	.95	.83	−.66	−.89	−.80
	50	.86	.89	.85	.77	−.51	−.78	−.78
	30	.75	.77	.74	.70	−.32	−.61	−.65
	10	.14	.12	.10	.15	.13	−.01	−.14
B	1,000	−0.06	−0.37	−0.55	−0.36	0.68	0.81	0.91
	850	−.04	−.39	−.64	−.48	.75	.91	.95
	700	−.04	−.40	−.68	−.53	.76	.93	.94
	500	−.05	−.42	−.69	−.53	.78	.93	.93
	400	−.08	−.42	−.68	−.50	.79	.92	.91
	300	−.10	−.43	−.58	−.32	.76	.82	.81
	250	−.13	−.20	−.04	.25	.33	.17	.19
	200	.05	.29	.62	.70	−.33	−.60	−.58
	150	.13	.47	.77	.71	−.55	−.79	−.79
	100	.14	.51	.76	.60	−.67	−.86	−.87
	50	.38	.73	.79	.63	−.38	−.58	−.63
	30	.52	.75	.61	.50	.03	−.13	−.19
	10	.48	.44	.21	.21	.41	.32	.29

TABLE 2.—*Radiance-geopotential height correlation matrix for (A) May–June 1969 and (B) October–November 1969*

	Pressure level (mb)	Channel (central wave number in cm^{-1})						
		669.3	677.8	692.3	699.3	706.3	714.3	750.0
A	1,000	−0.09	−0.10	−0.16	−0.27	−0.28	−0.08	0.03
	850	−.54	−.57	−.64	−.72	.06	.47	.63
	700	−.72	−.77	−.83	−.86	.30	.73	.84
	500	−.81	−.87	−.92	−.90	.49	.87	.89
	400	−.83	−.89	−.94	−.91	.55	.90	.88
	300	−.84	−.90	−.95	−.89	.61	.92	.86
	250	−.85	−.91	−.96	−.88	.64	.92	.85
	200	−.85	−.92	−.95	−.85	.68	.93	.83
	150	−.85	−.92	−.92	−.79	.71	.91	.81
	100	−.82	−.88	−.86	−.71	.71	.89	.78
	50	−.32	−.34	−.28	−.16	.46	.45	.36
	30	.35	.35	.37	.44	.08	−.15	−.24
	10	.44	.45	.44	.49	.04	−.26	−.41
B	1,000	0.00	−0.11	−0.30	−0.36	0.08	0.20	0.15
	850	−.01	−.27	−.54	−.51	.43	.61	.60
	700	−.02	−.34	−.63	−.55	.58	.78	.78
	500	−.03	−.38	−.69	−.58	.68	.88	.88
	400	−.02	−.38	−.67	−.56	.68	.87	.87
	300	−.05	−.41	−.70	−.56	.73	.91	.90
	250	−.05	−.42	−.70	−.55	.75	.92	.91
	200	−.05	−.42	−.69	−.51	.77	.92	.92
	150	−.04	−.40	−.65	−.44	.80	.92	.91
	100	−.01	−.36	−.57	−.35	.81	.89	.88
	50	.15	−.08	−.23	−.04	.71	.68	.68
	30	.33	.23	.08	.22	.62	.49	.47
	10	.47	.48	.26	.32	.54	.40	.35

TABLE 3.—*Radiance autocorrelation matrix for (A) May–June 1969 and (B) October–November 1969*

	Channel	669.3	677.8	692.3	699.3	706.3	714.3	750.0
A	669.3	1.00	0.96	0.92	0.83	−0.51	−0.78	−0.73
	677.8		1.00	.96	.87	−.58	−.84	−.77
	692.3			1.00	.94	−.55	−.87	−.82
	699.3				1.00	−.29	−.75	−.79
	706.3					1.00	.78	.50
	714.3						1.00	.88
	750.0							1.00
B	669.3	1.00	0.84	0.59	0.40	0.06	−0.05	−0.06
	677.8		1.00	.89	.71	−.14	−.36	−.41
	692.3			1.00	.89	−.30	−.60	−.64
	699.3				1.00	.02	−.38	−.45
	706.3					1.00	.87	.79
	714.3						1.00	.94
	750.0							1.00

The relatively high negative correlations between the SIRS radiances measured in some of the "more opaque" spectral intervals (that is, the 699.3, 692.3, 677.8, and 669.3 cm^{-1} channels) and tropospheric temperatures are noteworthy. This results from a well-known inverse correlation of lower stratospheric temperature with tropospheric temperature. These negative correlations are relatively unstable in that they are weaker in early fall than in late spring. As will be shown, this stratosphere-troposphere relation becomes important for deriving the tropospheric temperature distribution when clouds interfere with the radiances measured in the more transparent SIRS spectral intervals.

Table 2 shows similar correlations of SIRS CO_2 radiances with geopotential height. Again the significant negative correlations of the stratospheric SIRS radiances with middle and upper tropospheric heights are noteworthy. They indicate that the tropospheric distribution of geopotential height, as well as temperature, can be statistically inferred even in cloudy situations when the measured energies are restricted to the upper levels of the atmosphere.

Table 3 shows the autocorrelation of the radiance measured in the various CO_2 channels. These correlations result because the transmission weighting functions overlap various regions of the atmosphere (fig. 2) and because the temperature of various atmospheric levels is correlated with the temperature of the other atmospheric levels. The relatively large changes in the negative correlations with season reflects the instability of tropospheric-stratospheric temperature correlations.

Finally, table 4 shows the channels most highly correlated with the temperatures of various pressure levels, the channel correlation coefficients, the multiple correlation of temperature with the radiances measured in all channels, and the standard error of temperature specified through linear regression by the radiances measured in all spectral channels. As clearly shown, the eight SIRS radiances are most highly dependent on the temperatures of discrete pressure levels between the earth's surface and the middle stratosphere. It is this vertical independence of observation that allows a temperature profile to be determined.

As shown in table 4, the correlation coefficients are 0.90 or greater for most pressure levels below 30 mb, and the standard errors are generally less than 2°C. The relatively large standard errors of temperature near the earth's surface and tropopause are most likely due to the weak sensitivity of the radiance observation to small-scale vertical features. It is reemphasized that the magnitudes of the correlation coefficients and standard errors shown here are affected by radiosonde as well as radiance inaccuracies. The decrease in correlation with increasing height in the stratosphere (that is, above the 100-mb level) probably results from the loss of radiosonde accuracy with altitude, as well as the reduction in the atmospheric contribution to measured radiances.

Also shown in table 4 are the multiple correlations and standard errors obtained when the 714.3 and 750.0 cm^{-1} radiances are not employed. As will be explained later, these two radiances are not used to specify the temperature and geopotential height distribution in cloudy areas. Although the standard errors of the temperatures of middle and lower tropospheric levels are larger for the cloud situation, they are still acceptably low. The surprisingly low standard errors are a result of the high

TABLE 4.—*Radiance-temperature correlations and standard errors of radiance specified temperatures for (A) May–June 1969 and (B) October–November 1969*

	All channels				All channels except 714.3 & 750.0 (cm^{-1})				
Pressure level (mb)	Highest individual correlation		Multiple correlation	Standard error (°C)	Highest individual correlation		Multiple correlation	Standard error (°C)	Pressure level (mb)
	Channel (cm^{-1})	Correlation			Channel (cm^{-1})	Correlation			
A 1,000	899.3	0.97	0.97	1.3	899.3	0.97	0.97	1.4	1,000
850	750.0	.91	.93	2.4	899.3	.88	.93	2.6	850
700	714.3	.93	.96	1.6	899.3	.81	.95	1.8	700
500	714.3	.92	.96	1.3	706.3	.71	.96	1.4	500
400	714.3	.88	.95	1.4	706.3	.73	.95	1.5	400
300	714.3	.82	.93	1.5	706.3	.77	.92	1.6	300
250	706.3	.63	.79	1.9	706.3	.63	.77	2.0	250
200	699.3	.87	.92	1.8	699.3	.87	.92	1.9	200
150	692.3	.90	.93	1.9	692.3	.90	.93	2.0	150
100	692.3	.95	.97	1.1	692.3	.95	.97	1.1	100
50	677.8	.89	.91	1.2	677.8	.89	.90	1.2	50
30	677.8	.77	.80	1.0	677.8	.77	.79	1.0	30
10	669.3	.15	.36	2.6	669.3	.14	.36	2.6	10
B 1,000	899.3	0.95	0.95	2.5	899.3	0.95	0.95	2.5	1,000
850	750.0	.95	.95	2.3	899.3	.90	.94	2.6	850
700	714.3	.94	.97	1.8	899.3	.87	.96	2.0	700
500	714.3	.93	.97	1.6	899.3	.85	.97	1.6	500
400	714.3	.92	.96	1.7	899.3	.85	.95	1.7	400
300	714.3	.82	.88	1.7	899.3	.80	.88	1.7	300
250	706.3	.33	.73	2.1	706.3	.33	.73	2.1	250
200	699.3	.70	.90	2.0	699.3	.70	.90	2.0	200
150	692.3	.77	.94	1.9	692.3	.77	.94	2.0	150
100	692.3	.76	.94	1.6	692.3	.76	.94	1.7	100
50	692.3	.79	.87	1.5	692.3	.79	.87	1.5	50
30	677.8	.75	.86	1.7	677.8	.75	.86	1.7	30
10	669.3	.48	.73	3.1	669.3	.48	.73	3.1	10

correlation of middle and lower tropospheric temperatures with surface and upper tropospheric temperature.

Table 4 indicates that there are slight changes in the multiple correlations with season. The multiple correlations for the fall season are somewhat higher, but so are the standard errors of estimate. The slight increases in the multiple correlations and standard errors are due to the increase in the variance of atmospheric temperature. The larger standard errors in the troposphere also result, in some degree, from the loss of channel 3 (714.3 cm^{-1}) because of excessive noise during the latter part of November. As will be shown later, the loss of channel 3 greatly reduced the accuracy of the radiance-derived temperatures and geopotential heights.

3. DEVELOPMENT OF REGRESSION RELATION BETWEEN INFRARED RADIANCE AND ATMOSPHERIC TEMPERATURE AND GEOPOTENTIAL HEIGHT

TEMPERATURE REGRESSION EQUATIONS

For a nonscattering cloudless atmosphere in local thermodynamic equilibrium, the spectral radiance observed at the top of the atmosphere, $N(\nu)$, is given by

$$N(\nu)=B[\nu, T(p_s)]\tau(\nu, p_s)-\int_1^{\tau(\nu,p_s)} B[\nu, T(p)]d\tau(\nu,p) \quad (1)$$

where $B[\nu, T(p)]$ is the Planck function at wave number ν and temperature T,p is pressure and $\tau(\nu,p)$ is the fractional transmittance of the atmosphere between level p and the top of the atmosphere. The subscript s refers to surface values. Equation (1) can be approximated by numerical quadrature and written in the form

$$N_i'=\sum_{j=1}^{J} B_{i,j}'\Gamma_{i,j} \qquad i=1, 2, \ldots, I \quad (2)$$

where I is the number of different spectral radiance observations. $J-1$ is the number of quadrature pressure levels, and the prime denotes a deviation from a mean condition; that is,

$$N_i'=N(\nu_i)-N_0(\nu_i)=N_i-N_{0i},$$

and

$$B_{i,j}'=B[\nu_i,T(p_j)]-B_0[\nu_i,T(p_j)]=B_{i,j}-B_{0i,j} \qquad j<J,$$
$$B_{i,j}'=B[\nu_i,T(p_s)]-B_0[\nu_i,T(p_s)]=B_{i,j}-B_{0i,j} \qquad j=J$$

where the zero subscript refers to the mean condition. Also,

$$\Gamma_{i,j}=d\tau(\nu_i, p_j) \qquad j<J$$

and

$$\Gamma_{i,j}=\tau(\nu_i, p_s) \qquad j=J.$$

Utilizing first-order Taylor expansions about the mean condition

$$B_{i,j}'=\left(\frac{\partial B_{i,j}}{\partial T_j}\right)_0 T_j' \text{ and } N_i'=\left(\frac{\partial N_i}{\partial T_i^*}\right)_0 T_i^{*\prime}$$

where T_i^* is the brightness temperature corresponding

to the radiance N_i, one can express equation (2) as

$$T_i^{*\prime}=\sum_{j=1}^{J} T_j'\eta_{i,j} \tag{3}$$

where

$$\eta_{i,j}=\left(\frac{\partial B_{i,j}/\partial T_j}{\partial N_i/\partial T_i^*}\right)_0 \Gamma_{i,j}.$$

Writing (3) in matrix notation gives

$$\mathbf{t}_B'=\mathbf{t}'\mathbf{H} \tag{4}$$

where the matrix $\mathbf{H}=(\eta_{j,i})$; $j=1, 2, \ldots, J$; $i=1, 2, \ldots, I$; $\mathbf{t}_B'$ is a row vector of observed brightness temperature deviations from the mean conditions; and $\mathbf{t}'$ is a row vector of atmospheric temperature departures from their respective means. The direct solution of equation (4) for the temperature profile is

$$\mathbf{t}'=\mathbf{t}_B'\mathbf{H}^{-1}. \tag{5}$$

In reality, equation (5) is an impractical solution. In the first place, there are only eight different spectral radiance observations, so only eight pressure levels can be considered, leading to an ambiguous representation of the atmosphere's vertical structure. Secondly, the matrix $\mathbf{H}$ is ill-conditioned with respect to matrix inversion due to the relatively weak independence of the transmission functions; consequently, the direct solution given by (5) is usually unstable, especially when considering realistic observational errors in $\mathbf{t}_B'$. Also, the solution given by equation (5) is not unique since a variety of temperature profiles can be integrated to yield the observed radiance values to within the noise level of the sensor.

Rodgers (1966) suggested determining a statistically optimum solution (that is, optimum in the least squares sense) from a given set of radiance observations. Consider equation (5) in its general mathematical form

$$\mathbf{t}'=\mathbf{t}_B'\mathbf{A}. \tag{6}$$

The matrix $\mathbf{A}$ is defined as that matrix that gives the best least-squares solution for $\mathbf{t}$ in a statistical ensemble of simultaneously observed radiances and temperature profiles. Extending equation (6) to cover the entire statistical sample yields

$$\mathbf{T}'=\mathbf{T}_B'\mathbf{A} \tag{7}$$

where $\mathbf{T}'$ is a $(K\times J)$ matrix of observed atmosphere temperature departures from the sample temperature mean, and $\mathbf{T}_B'$ is a $(K\times I)$ matrix of simultaneously observed brightness temperature departures from their respective sample means. The index limit K refers to the total number of temperature profile-radiance sets in the statistical sample. The least-squares solution for the matrix $\mathbf{A}$ is then

$$\mathbf{A}=[(\mathbf{T}_B')^T\mathbf{T}_B']^{-1}\,(\mathbf{T}_B')^T\mathbf{T}' \tag{8}$$

where the superscript T indicates matrix transposition. The elements of $\mathbf{A}$ are simply regression coefficients. Any number of pressure levels can be considered. Once $\mathbf{A}$ is determined, it can be used routinely in the solution (6) for the temperature profile from arbitrary measurements of $\mathbf{t}_B'$.

It is instructive to gain an understanding of the physical significance of equation (8). It follows from (4) that the brightness temperature observations can be approximated by

$$\mathbf{t}_B'=\mathbf{t}'\ \mathbf{H}+\boldsymbol{\epsilon} \tag{9}$$

where $\boldsymbol{\epsilon}$ is a vector of the observational errors. Rewriting (9) to cover the statistical ensemble considered above gives

$$\mathbf{t}_B'=\mathbf{t}'\ \mathbf{H}+\mathbf{E}. \tag{10}$$

By substituting (10) into (8), it can be shown (see, for instance, Rodgers 1966 or Westwater and Strand 1968) that, assuming the observational errors are uncorrelated with atmospheric temperature and that cross products of E and T can be neglected,

$$\mathbf{A}=[\mathbf{H}^T(\mathbf{T}')^T\mathbf{T}'\ \mathbf{H}+\mathbf{H}^T\ \mathbf{E}]^{-1}\ \mathbf{H}^T(\mathbf{T}')^T\mathbf{T}' \tag{11}$$

where $\mathbf{E}^T\mathbf{E}$ is the covariance of the observational errors times $K-1$. It can be seen from (11) that the regression coefficients are a function of the atmospheric transmittances, the covariance of atmospheric temperatures, and the magnitude of the observational errors. Thus, for optimum results, the regression coefficient matrix should be allowed to vary with latitude and time to account for variations in the covariance of atmospheric temperatures. Furthermore, the current characteristics of the measurement errors should be adequately represented in the dependent sample used to derive the regression coefficients. Based upon these considerations, it is evident that best results will be obtained using a coefficient matrix derived from an observational sample covering a time period as close as possible to the time when the coefficient matrix is utilized for independent calculations.

GEOPOTENTIAL HEIGHT REGRESSION EQUATIONS

Studies concerning the statistical nature of geopotential height (in particular studies of Obukhov 1960, Holmström 1963, and Bradley and Wiin-Nielson 1968 on empirical orthogonal functions) suggest that the geopotential height profile, $Z(p)$, can be approximated accurately by the linear combination

$$Z(p)-Z_0(p)=Z'(p)=\sum_{i=1}^{I} C_i\phi_i(p) \tag{12}$$

where the empirical functions, $\phi_i(p)$, have been shown to be nearly invariant with respect to geographical position in time. It then follows from equation (12), the hydrostatic equation, and the gas law that

$$T'(p)=\sum_{i=1}^{I} C_i\chi_i(p) \tag{13}$$

where

$$\chi_i(p) = -g\, d\, \phi_i(p)/R\, d \ln P,$$

g is the acceleration of gravity, and R is the gas constant for dry air. Writing both (12) and (13) in matrix form yields

$$\mathbf{z}' = \mathbf{\Phi c} \tag{14}$$

and

$$\mathbf{t}' = \mathbf{X c} \tag{15}$$

where $\mathbf{\Phi} = (\phi_{j,i})$ and $\mathbf{X} = (\chi_{j,i})$. Equations (14) and (15) may be combined to give

$$\mathbf{t}' = \mathbf{X}(\mathbf{\Phi}^T\mathbf{\Phi})^{-1}\ \mathbf{\Phi}^T\ \mathbf{z}' = \mathbf{X}\ \mathbf{\Phi}^T\ \mathbf{z}' = \mathbf{D}\ \mathbf{z}' \tag{16}$$

where the least-squares solution for $\mathbf{c}$ has been applied to (14). It follows from (16) that, if the number of pressure levels does not exceed the number of empirical functions (that is, $J \leq I$ such that $\mathbf{D}^{-1}$ is nonsingular),

$$\mathbf{z}' = \mathbf{D}^{-1}\ \mathbf{t}'. \tag{17}$$

Equation (17) states that the geopotential height profile is uniquely related to the temperature profile. Consequently to the extent that (12) is valid, the geopotential height distribution can be specified solely from the temperature profile. This result conflicts with theoretical reasoning, for it is known from hydrostatic considerations that in order to calculate the geopotential height profile from the temperature profile it is necessary to specify a base height of some pressure level. It has been shown by Smith and Fritz (1969), however, that the geopotential height profile is statistically correlated with the temperature profile, as is also evident from the correlations shown in table 2. They show very high correlations of upper tropospheric heights with middle tropospheric and lower stratospheric temperatures. This result indicates that useful statistical height estimates can be obtained in the absence of a prespecified pressure-height reference (that is, an adequate pressure-height reference can be statistically estimated from the temperature profile).

The geopotential height profile can be expressed as a function of the satellite-measured radiances. Substituting equation (16) into (4), one obtains the relation

$$\mathbf{t}_B' = \mathbf{zDH} \tag{18}$$

and the solution

$$\mathbf{z}' = \mathbf{t}_B'(\mathbf{DH})^{-1} = \mathbf{t}_B'\mathbf{B}. \tag{19}$$

The matrix $(\mathbf{DH})^{-1}$ exists only if the number of pressure levels equals the number of spectral radiance observations. However, treating B as a regression matrix, it can be determined from a statistical sample of simultaneously observed brightness temperatures and geopotential heights using the least-squares solution

$$\mathbf{B} = [(\mathbf{T}_B')^T(\mathbf{T}_B')]^{-1}(\mathbf{T}_B')^T\mathbf{Z}'. \tag{20}$$

Thus, any arbitrary number of pressure levels can be considered. Once B is determined, it can be used routinely in the solution (19) for the geopotential height profile from arbitrary measurements of $\mathbf{t}_B'$.

BASE CORRECTION

The solution given by equation (19) implicitly contains a statistical pressure-height base condition. However, over many regions of the earth, adequate surface observations exist to provide a direct measure of the height of some pressure level (for example, the 1000-mb level). Such a pressure-height reference can be used to correct the statistically estimated profile.

If the height of some pressure level is known, a correction quantity, K, may be determined from the difference between the observed height of some reference pressure, p_r, and the statistically estimated height. Thus, the correction is given by

$$K = Z(p_r) - \hat{Z}(p_r)$$

where the circumflex denotes the statistical estimate obtained from (19). Since the base height error should be the same at all levels, the correction K can simply be added to the statistical heights obtained for all pressure levels. It can be shown that the corrected solution is nearly equivalent to the height profile obtained by integrating the hydrostatic equation from the reference pressure level using the radiance-calculated temperature profile.

ACCOUNTING FOR NONLINEARITIES

The regression equations derived above are linear. The linearity was imposed by the linear Taylor approximations and the assumption of temperature-independent transmission functions. The linear Taylor approximation becomes poor for conditions greatly different from the mean states. It is known that the transmission functions are variable with temperature (fig. 1). (It is noted that the transmission functions vary significantly with water vapor as well, but this variation can usually be explained as a function of temperature due to the high correlation of water vapor content with temperature.)

Theoretical and empirical studies have shown that these nonlinearities are adequately accounted for in simple second-order regression relations. These relations have the same form as given earlier except that the squares of the observed brightness temperatures are included as predicting observations. The vector $\mathbf{t}_B'$ in the equations given above is replaced by a vector having twice as many elements as the number of spectral radiance observations; half of this vector is composed of spectral radiance brightness temperature deviations, while the other half is composed of the squares of these spectral radiance brightness temperature deviations.

4. CORRECTION FOR CLOUDINESS, HIGH TERRAIN, AND HOT TERRAIN

When determining and applying the coefficient matrices

of the regression relations derived above, it is necessary to remove the influences of clouds, high terrain, and hot terrain on the observed radiances. This is necessary since:

1) The atmospheric transmission function for each spectral interval is assumed to be constant. Perturbations due to variations in nongaseous absorbers (for example, dust, clouds, etc.) are not accounted for in the regression relations.

2) The surface of the earth is assumed to be at a fixed pressure level (that is, 1000 mb).

3) Due to the lack of routine conventional observations of ground temperature, it must be assumed that the shelter temperature and ground temperature are equal.

In reality, however, there are large departures from this observational situation. Thus, it is necessary to correct the radiance observations to radiances that would have been observed under the observational situation assumed above. The corrected observations are used to derive the regression relations and to retrieve profiles with these relations.

CORRECTIONS FOR CLOUDINESS

Clouds generally exist within the relatively large field of view (that is, 225 km square) of SIRS. Consequently, it is usually necessary to correct the measured radiances for the effects of clouds. The corrected measurements, called "equivalent clear column radiances," can then be related to the temperature profile. Since the corrections depend upon the height and amount of cloud within the field of view as well as on the temperature profile, an iterative solution must be employed to retrieve temperature profiles from cloud-contaminated radiance observations.

Multilevel cloudiness can exist within the field of view of the SIRS. A common atmospheric situation is one in which a semitransparent cirrus exists over opaque middle clouds. Therefore, a two-level cloud model has been developed and utilized to describe the cloud distribution from SIRS radiances and subsequently to compute the radiance corrections needed to determine the temperature profile.

The radiances measured over an atmosphere containing no more than two levels of clouds can be shown to be given by

$$\begin{aligned} N(\nu)=&B[\nu, T(p_s)]\tau(\nu, p_s)-\int_0^{p_s} B[\nu, T(p)]d\tau(\nu, p) \\ &-A_U\left\{B[\nu, T(p_s)]\tau(\nu, p_s)-B[\nu, T(p_u)]\tau(\nu, p_u)\right. \\ &\qquad\left.-\int_{p_u}^{p_L} B[\nu, T(p)]d\tau(\nu, p)\right\} \\ &-A_L(1-A_U)\left\{B[\nu, T(p_s)]\tau(\nu, p_s)\right. \\ &\left.-B[\nu, T(p_L)]\tau(\nu, p_L)-\int_{p_L}^{p_s} B[\nu, T(p)]d\tau(\nu, p)\right\} \end{aligned} \quad (21)$$

where the subscripts U and L refer to upper and lower level cloud conditions and A is the fractional radiative cloud amount defined as the product of the fractional cloud cover and fractional transmittance of the cloud. In equation (21), it is assumed that the upper level cloud is randomly distributed with respect to the lower level cloud (that is, the breaks in any upper level clouds are uncorrelated with the breaks in any lower level clouds). Any violation of the random distribution assumption breaks down the physical interpretation of the A_U and A_L cloud parameters but does not destroy the parametric relation given by (21). Therefore, A_U and A_L must be considered as effective fractional radiative cloud amounts that can usually be interpreted as true fractional cloud amount when only a single level of opaque clouds exists.

It follows from equation (21) that

$$N_C(\nu)=N(\nu)+A_UX[\nu,P_U,P_L,T(p)]+A^*Y[\nu,P_L,T(p)] \quad (22)$$

where $N_C(\nu)$ is the radiance that would be measured if the atmosphere was clear (that is, the equivalent clear column radiance), $N(\nu)$ is the measured radiance, $X[\nu,P_U,P_L,T(p)]$ is the first term of equation (21) in braces, $Y[\nu,P_L,T(p)]$ is the second term in braces, and $A^*=A_L\cdot(1-A_U)$. The correction $C(\nu)$ that must be added to the measured radiances to produce equivalent clear column radiances, from which the temperature profile can be calculated, is then given by

$$C(\nu)=A_UX[\nu,P_U,P_L,T(p)]+A^*Y[\nu,P_L,T(p)]. \quad (23)$$

In computing the corrections, $C(\nu)$, clouds are allowed to exist at any two-level combination of the standard pressure levels[1] below 150 mb (that is, 200 and 250, 200 and 300, . . . , 200 and 850; 250 and 300, 250 and 400, . . . , 250 and 850, etc.). When given an estimate of the temperature profile, the equivalent clear column radiances for the three channels most sensitive to clouds, the 714 cm^{-1}, 750 cm^{-1}, and 899 cm^{-1} channels, can be computed using equation (1). An estimate of the corrections for these channels, $C(\nu)$, implied by the estimated temperature profile is then given by

$$\hat{C}(\nu)=\hat{N}_C(\nu)-N(\nu) \quad \nu=714, 750, 899 \text{ cm}^{-1} \quad (24)$$

where $N_C(\nu)$ is the clear column radiance calculated from (1) and $N(\nu)$ is the measured radiance. The X and Y terms of equation (23) are also specified for all allowable combinations of upper and lower level cloud pressures using the estimated temperature profile. Substituting $\hat{C}(\nu)$ obtained from (24) for $C(\nu)$ in (23) for the 714 cm^{-1} and 899 cm^{-1} intervals, A_U and A^* are calculated for all upper and lower cloud level combinations. This calculation is merely a solution of the two simultaneous linear equations given by (23) (one for $\nu=714$ cm^{-1} and one for $\nu=899$ cm^{-1}) for the unknowns A_U and A^*. Different values of A_U and A^* are obtained for the different pressure level combinations.

[1] The standard pressure levels are the 10-, 30-, 50-, 100-, 150-, 200-, 250-, 300-, 400-, 500-, 700-, 850-, and 1000-mb levels.

Based upon physical considerations, A_U and A^* calculations are restricted to a range of values between zero and unity (that is, if A_U or A^* is calculated to be greater than unity, it is set equal to unity and if A_U or A^* is calculated to be less than zero, it is set equal to zero).

The most probable upper level and lower level cloud condition is then determined from the radiance measured in the 750 cm^{-1} channel. Using $C(\nu)$ from (23), for $\nu=750$ cm^{-1}, and $\hat{C}(\nu)$ from (24), for $\nu=750$ cm^{-1}, the most probable cloud condition is specified as that in which

$$|C(\nu)-\hat{C}(\nu)|=\min \quad \nu=750 \text{ cm}^{-1}.$$

Once the cloud condition is specified, the equivalent clear column radiances for the remaining spectral channels can be determined from equation (22).

It is noted that, if only a single layer of clouds exists, either A_U or A_L will be calculated as zero. Also if one is forced to consider only a single layer of clouds, due, say, to the degradation of radiance accuracy in the 714 cm^{-1}, 750 cm^{-1}, or 899 cm^{-1} channels, cloud corrections can still be estimated using the above procedure by setting A_U equal to zero in equations (22) and (23). A^* or A_L in this case is then calculated using a single radiance observation (that is, $A^*=A_L=C(\nu)/Y[\nu, P_L, T(p)]$.

Computing equivalent clear column radiances from the dependent sample of observations to be used to compute the regression coefficient matrices is straightforward since the temperature profile is known. The quantities $X[\nu,P_U, P_L,T(p)]$ and $Y[\nu, P_L, T(p)]$ are calculated using the observed temperature profile. Subsequently, the cloud conditions and equivalent clear column radiances can be specified directly from the radiance observations.

When the temperature profile is to be determined from the radiances, an iterative retrieval procedure must be employed in cloudy situations. The retrieval procedure utilizes an estimate of surface (shelter) temperature and six-channel regression coefficient matrices derived without the 714 cm^{-1} and 750 cm^{-1} channel equivalent clear column radiances. (The 714 cm^{-1} and 750 cm^{-1} radiances are used to specify the cloud conditions.)

In practice, a prespecified surface temperature is compared with the brightness temperature observed in the window, 899.3 cm^{-1}, channel. If the observed window brightness temperature and surface temperature are within 5°C of each other, the atmosphere is assumed to be clear, and all the observed radiances are used with eight-channel regression matrices to specify the temperature and geopotential height profiles. If the observed window brightness temperature is more than 5°C lower than the surface temperature, clouds are assumed to exist, and cloud corrections must be made. (When the observed brightness temperature is more than 5°C higher than the surface temperature, the atmosphere is assumed to be clear but "hot terrain" corrections, as described later, must then be made.)

In the cloudy situation, an initial estimate of the equivalent clear column radiances for the five most opaque CO_2 channels is obtained by assuming zero cloud contamination (that is, $N_C(\nu)=N(\nu)$; $\nu=669.3$, 677.8, 692.3, 699.3, 706.3). With the initial estimate of the equivalent clear column radiance for the window channel, 899.3 cm^{-1}, based on the prespecified surface temperature, they are used in the six-channel regression relations to specify a "first guess" temperature profile. This initial temperature profile will tend to be colder than the true profile, the magnitude of the discrepancy depending on the degree to which the CO_2 radiances are influenced by the clouds. The prespecified surface temperature restrains the first guess profile from being unrealistically "cold" near the earth's surface.

Using this first guess temperature profile, cloud parameters and corrections are estimated using the procedure given above. Improved estimates of the equivalent clear column radiances are used in the six-channel regressions to obtain an improved estimate of the temperature profile. The procedure is iterated until the cloud corrections cease to change from one iteration to the next.

The sequence of iterated solutions is always from cold to warm; thus the corrections vary from zero to positive values. Convergence is almost always achieved within four iterations, even for high cloud conditions.

It should be emphasized that clouds do not usually transmit any radiation emitted from below. Consequently in cloudy sky conditions, the temperature profile information inherent in the radiance observations is mainly restricted to the atmosphere above the clouds. The temperatures inferred below the clouds result largely from the statistical relation of these temperatures with those observed above the clouds and at the surface.

Figure 3 shows an example of a temperature profile retrieval when significant cloudiness existed within the SIRS field of view. As shown, the first guess is more than 10° too low in a portion of the troposphere, as indicated by comparison with conventional radiosonde data. The cold guess was due to the unaccounted-for cloud influence on the radiances measured in the 699 cm^{-1} and 706 cm^{-1} channels. The final solution obtained in four iterations, however, is in excellent agreement with radiosonde data.

CORRECTION FOR HIGH TERRAIN

High terrain corrections are calculated and applied in a manner similar to the cloud correction procedure. The radiative departures from sea-level conditions produced by high terrain are assumed to be equivalent to the radiative departures from clear sea-level conditions produced by a cloud existing at the terrain elevation.

In practice, the known height of the earth's surface is used to determine whether a terrain correction is necessary. When the terrain is higher than 40 decameters above sea level, the prespecified "observed" surface temperature is replaced by an extrapolated sea-level temperature. The effective pressure-height and amount of the high terrain, as well as any upper level clouds, filling the field of view

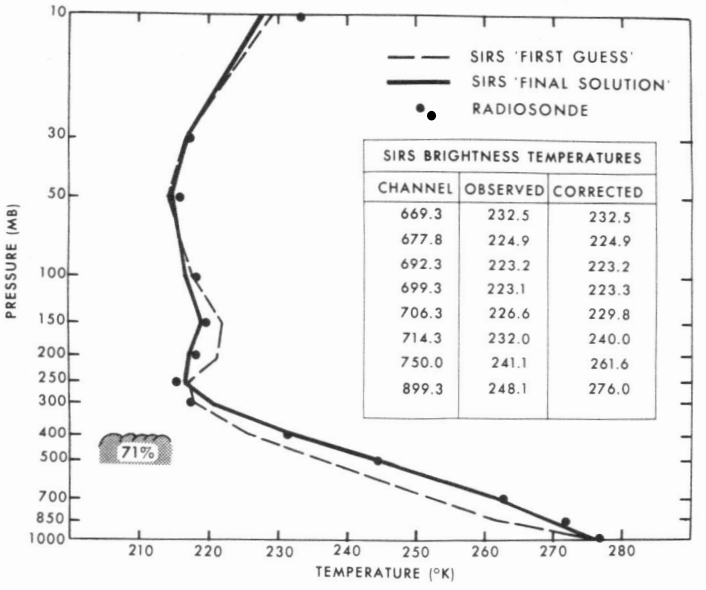

FIGURE 3.—Comparison of SIRS temperature profile with a coincident radiosonde observation in partially cloudy sky conditions. The initial and final steps of the cloud iterative solution are illustrated.

are calculated using the cloud correction procedure, the terrain being treated as the lower level cloud. (The two-level cloud model is capable of treating one level of clouds above the high terrain.) As in the cloud situation, a statistically extrapolated profile is obtained below the terrain level down to the 1000-mb level.

CORRECTION FOR HOT TERRAIN

If the ground is warmer than the air temperature near the surface, a correction must be applied to the measured radiances before atmospheric temperatures can be derived. This is necessary to alleviate the erroneous interpretation of radiances that the lower troposphere is very warm when in truth only the ground is relatively "hot." The correction for each channel takes the form

$$K(\nu)=\{B[\nu,T_{sh}]-B[\nu,T_g]\}\ \tau(\nu,p_s)$$

where $K(\nu)$ is the correction quantity (negative), T_{sh} is the shelter temperature, and T_g is the ground temperature.

In practice, T_g is estimated from brightness temperature observed in the "window" channel while T_{sh} is obtained from conventional surface temperature analyses, as outlined in the next section. When T_g exceeds T_{sh} by more than 5°C, the correction $K(\nu)$ is computed and added to the measured radiances. The correction is assumed to be zero when the window brightness temperature is less than 5°C above the estimated shelter temperature.

5. COMPUTATIONAL PROCEDURES

DERIVATION OF REGRESSION COEFFICIENTS

For the Northern Hemisphere, the regression coefficients given by equations (8) and (20) are computed using standard pressure level temperature and geopotential heights obtained from 00 GMT and 12 GMT objective analyses of conventional radiosonde data and Nimbus 3 SIRS-observed radiances. The objective analyses are prepared operationally by the National Meteorological Center (NMC). The grid-point analysis data are interpolated bilinearly in space and linearly in time to the locations and observation times of the SIRS measurements, providing sets of SIRS radiances and "coincident" temperature and geopotential height profiles. Initially, only portions of the analyses and satellite data close to radiosonde stations were used for computing the regression coefficients.

The conventional and SIRS data sets are used to compute regression coefficients for three different latitude zones of the Northern Hemisphere: 18° N.–40° N., 35° N.–55° N., and 50° N.–80° N. The lowest latitude, 18° N., is close to the southern boundary of the NMC analyses. The highest latitude, 80° N., is the highest latitude in which SIRS observations can be made, owing to the orbital inclination of the Nimbus 3 satellite. The zones are overlapped to alleviate the occurrence of discontinuities across zone boundaries when the regression coefficients are used for independent calculations.

The regression data samples for each zone are restricted to 700 sets of data. This limits the observation period to about 2 weeks. The regression data sample is updated every few days, providing a sample period close to the time when the independent profile calculations are made using observed radiances.

Due to the sparsity of conventional data and the lack of operational analyses, a sampling procedure different from that discussed above has to be employed for the Southern Hemisphere. Only two zones are considered: 18° N.–25° S. and 20° S.–80° S. The sample sets consist of radiosonde data and satellite observations obtained within 6 hr and 200 mi of the radiosonde station. Although the time and space continuity tolerances of the conventional and satellite data seem less than satisfactory, they are necessary to enable sufficient statistical samples to be obtained. The sample sizes are restricted to 500 sets of observations which in turn limit the sample period to about 6 weeks.

The statistical regression coefficients for the 20° S.–80° S. zone are derived in terms of departures from zonal means. (The zonal mean of each variable is specified using regressions based on the sine of latitude and sine of latitude squared.) The regression relations derived in this manner were found adequate to retrieve the variety of atmospheric conditions that exists between 20° S. and 80° S. using a single set of regression coefficients.

The steps taken to compute the regression coefficients can be summarized as:

1) Samples of upwelling radiance observations and coincident conventional temperature and geopotential height profile observations are obtained in the manner described above.

TABLE 5.—*Regression coefficients computed for September 1969 (35° N.–55° N.)*

A. Sample Mean Brightness Temperatures

ν_i(cm^{-1})	899.3	750.0	714.3	706.3	699.3	692.3	677.8	669.3
$\overline{T}_B$(°K)	290.5	273.1	248.1	235.9	226.6	224.2	225.9	233.5

B. Sample Mean Temperature and Temperature Regression Coefficients

P_j	$\overline{T}$(°K)	a_1	a_2	a_3	a_4	a_5	a_6	a_7	a_8	a_1'	a_2'	a_3'	a_4'	a_5'	a_6'	a_7'	a_8'
1,000	292.1	.46	.64	-.10	-1.28	2.01	-2.22	.67	.02	.007	-.021	-.073	.099	-.077	.221	-.202	.157
850	286.0	.16	.50	1.25	-.50	-.50	.22	-1.17	1.03	.005	-.013	-.009	-.180	-.170	.052	.120	.067
700	276.6	.03	.18	1.07	.41	-.65	-.85	-.19	.59	.002	-.008	.001	-.109	-.008	.041	.045	-.022
500	260.2	.02	-.10	.86	.94	-.23	-1.66	.74	.31	-.001	-.009	-.011	.037	.051	-.087	.036	.143
400	248.6	.04	-.28	.89	.78	.94	-2.72	1.15	.26	.005	-.016	-.036	.124	.060	-.118	.048	.120
300	233.2	.04	-.25	.45	.66	2.41	-3.24	.54	.58	.003	-.010	-.019	.112	.272	-.188	.116	-.042
250	225.5	.04	-.12	.12	-.21	4.54	-2.64	-.88	.42	-.005	.012	.033	-.038	.410	-.101	.053	-.259
200	220.7	.04	.04	.07	-1.22	3.78	1.31	-2.44	-.29	-.010	.022	-.014	-.053	-.188	.098	-.003	-.008
150	217.2	.02	.11	-.09	-1.01	.49	3.39	-1.42	-.58	.000	.005	.012	-.075	.067	-.156	.040	.172
100	214.3	-.03	-.07	-.27	-.03	-1.32	2.16	.88	-.44	.003	-.001	.030	-.031	.156	-.045	-.115	.060
50	218.0	-.04	-.24	.36	.36	-.50	.11	1.60	-.49	-.001	.004	-.004	-.039	-.098	.132	-.050	-.070
30	221.7	-.01	-.11	.39	.07	.18	-.36	1.15	-.31	-.001	.005	-.020	-.048	.051	-.011	.085	-.086
10	233.9	-.04	.07	.04	-.13	.50	-.62	-.13	.60	-.001	-.004	.033	-.161	.009	.085	-.072	.061

C. Sample Mean Geopotential Height and Geopotential Height Regression Coefficients

P_j	$\overline{Z}$(m)	b_1	b_2	b_3	b_4	b_5	b_6	b_7	b_8	b_1'	b_2'	b_3'	b_4'	b_5'	b_6'	b_7'	b_8'
1,000	120	-2.74	4.54	-26.12	6.81	-7.50	-27.00	-.81	13.53	.023	-.122	1.990	-1.778	4.783	-2.385	-2.231	1.625
850	1503	-1.04	7.85	-23.14	1.36	-4.21	-29.96	-5.74	19.37	.068	-.196	1.868	-2.191	5.192	-2.751	-1.864	2.315
700	3106	-.46	9.46	-15.67	.55	-7.60	-32.58	-9.01	23.74	.097	-.300	1.780	-2.912	4.555	-2.322	-1.452	2.673
500	5755	-.43	9.38	-6.12	8.38	-12.37	-45.52	-5.58	27.50	.085	-.370	1.589	-3.021	4.522	-2.031	-1.448	3.380
400	7418	-.36	7.89	-.50	15.14	-9.79	-60.66	.32	29.41	.123	-.447	1.383	-2.796	4.480	-2.662	-1.333	4.762
300	9448	-.04	5.83	4.56	22.45	2.90	-84.98	7.01	33.27	.181	-.619	1.335	-1.723	5.167	-3.728	-.993	5.305
250	10671	.07	4.55	5.64	25.19	22.89	-101.14	5.62	36.12	.174	-.597	1.547	-1.935	6.391	-4.589	-.499	4.495
200	12128	.41	4.50	6.10	19.44	52.40	-108.46	-4.78	37.53	.105	-.450	1.459	-1.894	6.926	-4.324	-.375	3.277
150	13973	.64	5.48	6.76	7.47	73.08	-86.61	-22.41	32.64	.060	-.327	1.403	-2.453	6.252	-5.272	1.175	2.978
100	16521	.88	4.72	7.83	-.26	59.63	-44.28	-28.64	26.16	.053	-.210	1.047	-2.665	7.652	-5.214	-.485	5.211
50	20911	.22	2.95	2.99	1.79	34.37	-11.69	-9.86	15.46	.036	-.222	1.820	-2.032	7.995	-5.574	-1.452	5.201
30	24201	-.11	.52	7.55	6.83	30.82	-15.29	14.27	5.90	.054	-.129	1.471	-3.147	7.666	-4.859	-.929	4.187
10	31533	-.17	-.66	17.08	2.71	40.26	-27.91	31.76	5.15	-.058	.339	-.520	-3.850	7.434	-2.421	-1.335	4.179

2) Corrections for clouds, high terrain, or hot terrain are calculated and applied to the observed radiances. The corrected radiances are then converted to brightness temperatures using the Planck equation.

3) The brightness temperatures and conventional data are grouped into the various latitude zones. For each zone, two sets of regression coefficients are computed for both temperature and geopotential height. One set is based on six channels of brightness temperature (that is, the 669.3, 677.8, 692.3, 699.3, 706.3, and 899.3 cm^{-1} channels) while the other set is based on all eight channels.

4) Finally, the six- and eight-channel regression coefficients and sample mean values for each zone are stored for subsequent independent calculations of temperature and geopotential height profiles from SIRS-observed radiances.

Table 5 shows an example of temperature and geopotential height regression coefficients and the sample mean temperatures, geopotential heights, and brightness temperatures derived from September data obtained between 35° and 55° N. For clear-sky conditions, they can be used to compute temperatures and geopotential heights using equations (6) and (19), written in the forms

$$T(p_j)=\overline{T}(p_j)+\sum_{i=1}^{8} a(\nu_i, p_j)[T_B(\nu_i)-\overline{T}_B(\nu_i)] + \sum_{i=1}^{8} a'(\nu_i, p_j)[T_B(\nu_i)-\overline{T}_B(\nu_i)]^2$$

and

$$Z(p_j)=\overline{Z}(p_j)+\sum_{i=1}^{8} b(\nu_i, p_j)[T_B(\nu_i)-\overline{T}_B(\nu_i)] + \sum_{i=1}^{8} b'(\nu_i, p_j)[T_B(\nu_i)-\overline{T}_B(\nu_i)]^2.$$

SPECIFICATION OF TEMPERATURE AND GEOPOTENTIAL HEIGHT PROFILES

As indicated earlier, to make independent calculations of the temperature and geopotential height profiles from observed radiances using the regression coefficients, one must obtain an initial estimate of the surface temperature to determine any necessary corrections for clouds, high terrain, or hot terrain. An adequate estimate of the surface temperature is obtained from the latest surface analysis, which is always within 12 hr of a SIRS observation. This surface temperature is extrapolated to the exact time of the SIRS observation using the diurnal trend indicated by surface analyses constructed on the previous day.

The procedure for calculating the temperature and geopotential height profiles can now be summarized. The surface temperature estimated for the time and location of a SIRS measurement is compared with the brightness temperature observed in the 899.3 cm^{-1} window channel. If the surface radiating temperature indicated by the window observation is within 5°C of the surface temperature, the temperature and geopotential height profiles are calculated directly from the observed brightness tempera-

397-749 O—70——5

tures using the eight-channel regression equations. If the surface radiating temperature indicated by the window channel exceeds the shelter temperature by more than 5°C, "hot ground" corrections are calculated and applied to the observed radiances. The temperature and geopotential height profiles are then calculated from the corrected brightness temperatures using the eight-channel regression equations. When the surface radiating temperature indicated by the window channel is more than 5°C lower than the surface temperature, the temperature and geopotential height profiles are calculated by the iterative procedure given earlier using the six-channel regression equations.

In the Northern Hemisphere where an adequate coverage of surface observations exists, the conventionally analyzed 1000-mb height field is used to correct (or "tie down") the SIRS statistically derived heights.

The procedures outlined above have been implemented with Northern Hemisphere SIRS observations on a routine operational basis since May 20, 1969. Southern Hemisphere implementation up to now has not been routine due to the lack of surface temperature observations. Southern Hemisphere retrievals are obtained on an experimental basis using climatological surface temperatures.

6. RESULTS

SOME TYPICAL COMPARISONS WITH RADIOSONDES

Figures 4 and 5 show comparisons of SIRS radiance-derived temperature profiles with radiosonde-observed temperature profiles over Berlin, Germany. As can be seen, the agreement shown in figure 4 is good at all levels. Figure 5, however, shows some disagreement in the tropopause region. The shallow and abnormally cold tropopause layer was not specified very well with the SIRS radiances. This inability is evidently due to the fact that this tropopause feature is both statistically anomalous and below the vertical resolution inherent in the radiation observations.

In the Southern Hemisphere, the accuracy of the SIRS soundings is presently degraded in the troposphere due to the lack of accurate surface temperature observations. As mentioned earlier, surface temperatures must be specified to obtain solutions in cloud areas. At present, inadequate seasonal normal surface temperatures are being used for the Southern Hemisphere profile calculations. In the near future, Southern Hemisphere surface temperatures will be obtained from high resolution infrared window observations (Smith et al. 1970). When using actual surface temperature observations, the accuracy of the profiles derived in the Southern Hemisphere should be comparable to that achieved in the Northern Hemisphere.

Figures 6, 7, and 8 show comparisons of tropical, midlatitude, and Antarctic radiosonde measurements with soundings obtained from Southern Hemisphere

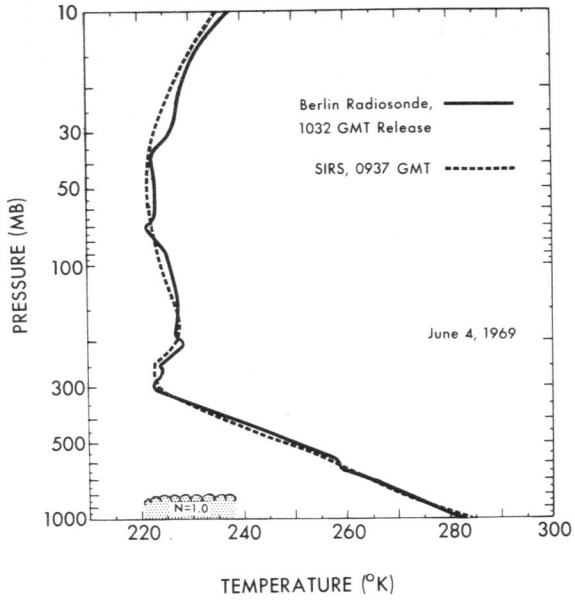

FIGURE 4.—Comparison of a SIRS-calculated and a radiosonde-observed temperature sounding over Berlin, Germany. An overcast (denoted as $N=1.0$) was determined from the SIRS radiances to exist at the 850-mb level.

SIRS observations. Agreement obtained in the upper troposphere and stratosphere is relatively good. Again it is shown that small-scale vertical features, such as inversions aloft, cannot be retrieved from the infrared radiance observations.

Many other comparisons of SIRS soundings with radiosonde observations have shown good compatibility above clouds in the troposphere and in the lower stratosphere. Frontal inversions and other small-scale vertical features are not detectable, but tropopause pressure and low-level surface inversions are retrieved quite well from the satellite radiance observations, especially under clear-sky conditions.

EXAMPLES OF USEFULNESS IN NUMERICAL ANALYSIS AND FORECASTING

Although the SIRS was flown as an experiment, its successful performance has permitted its data to be utilized conservatively, but routinely, in the Northern Hemisphere numerical analysis and forecast operation. Limited samples of SIRS data have been used to construct Southern Hemisphere analyses.

Figures 9 and 10 show profiles of 500-mb and 200-mb heights observed by the SIRS along the orbital track of the Nimbus 3 satellite. There is generally close agreement between the SIRS statistically derived heights (shown as solid dots) with the National Meteorological Center (NMC) analysis of conventional radiosonde-derived heights. The dashed curves indicate that an improvement is obtained by correcting the statistical heights using an observed pressure-height reference (in this case the analyzed 850-mb height).

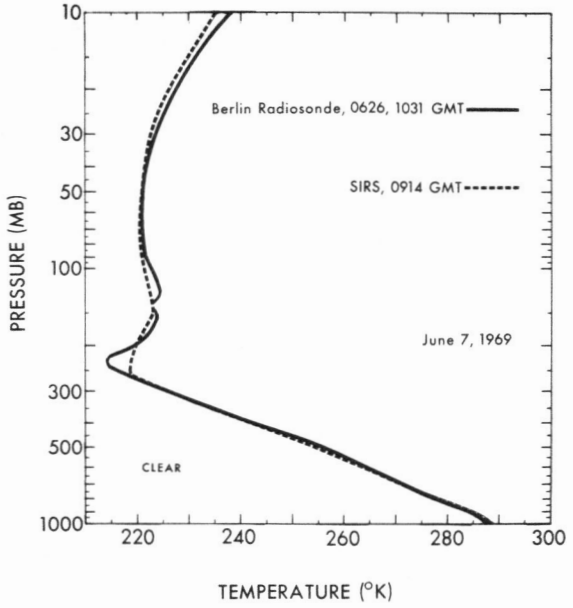

FIGURE 5.—Comparison of a SIRS-calculated and a radiosonde-observed temperature sounding over Berlin, Germany.

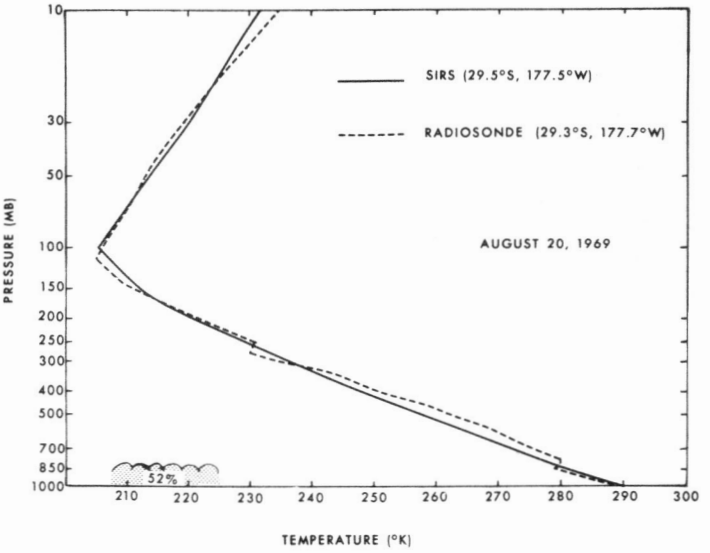

FIGURE 6.—Comparison of a SIRS-calculated and radiosonde-observed "tropical" temperature profile.

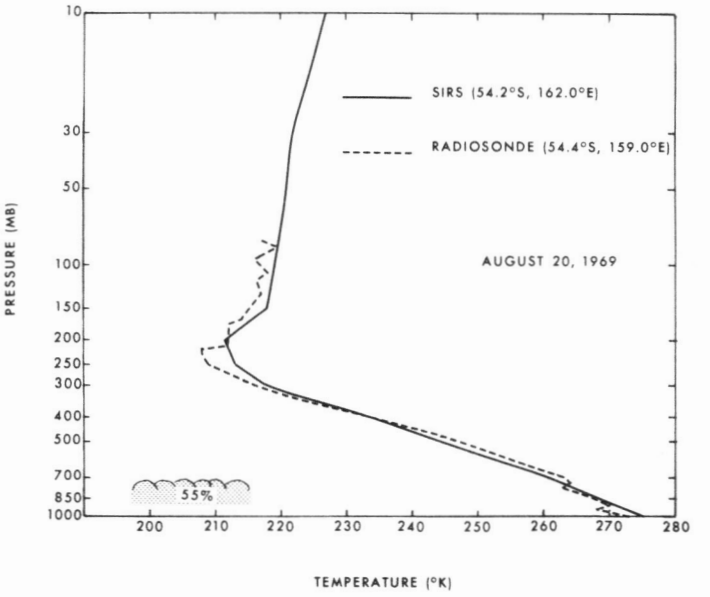

FIGURE 7.—Comparison of a SIRS-calculated and radiosonde-observed "temperate" temperature profile.

The major potential of satellite soundings is to improve the analysis over areas with sparse conventional data coverage, and subsequently to improve the forecast. The National Meteorological Center currently uses the SIRS data in its operational objective analyses. Many cases have been found where the SIRS soundings differ significantly from the first guess (12-hr forecast) used for the objective analysis in areas of sparse conventional data. In such cases, it is usually necessary to manually "bogus" observations around the SIRS soundings to force the objective analysis to draw for the satellite data. The bogusing is required because of the large gaps between orbital tracks of the satellite. Without the bogusing, the objective analysis system does not always yield a final analysis that agrees with the satellite soundings. This problem will be partially alleviated with future satellite sounders that are designed to observe between the orbital tracks as well as along them.

Several experiments have been conducted to assess the possible improvement of the forecast due to the addition of satellite data to the existing conventional network of observations. The first experiment consisted of running 24-, 48-, and 72-hr forecasts from two different initial conditions: 1) the objective analysis obtained from conventional data only and 2) the objective analysis obtained with SIRS and conventional data. The two initial conditions were obtained from observations on June 24, 1969.

Figure 11 shows the differences in the 500-mb analyses constructed with and without SIRS data over the mid-Pacific. In this region, the primary difference in the analysis produced by the SIRS soundings is the increase in the magnitude of the heights and the increase in the speed of the westerlies across the northern portion of a trough at 175° W., leaving a cutoff low center at 35° N. As shown, the largest absolute differences were only 12 decameters.

Figure 12 shows the differing 24-hr prognoses that resulted from the two initial analyses. The main difference lies in the improved forecast of the intensification of the trough off the northwest coast of the United States. This difference is shown more dramatically in the 48-hr 500-mb forecast, figure 13. Here, the separate low center off the northwest coast was predicted from the initial analysis with SIRS data, but not from the conventional analysis.

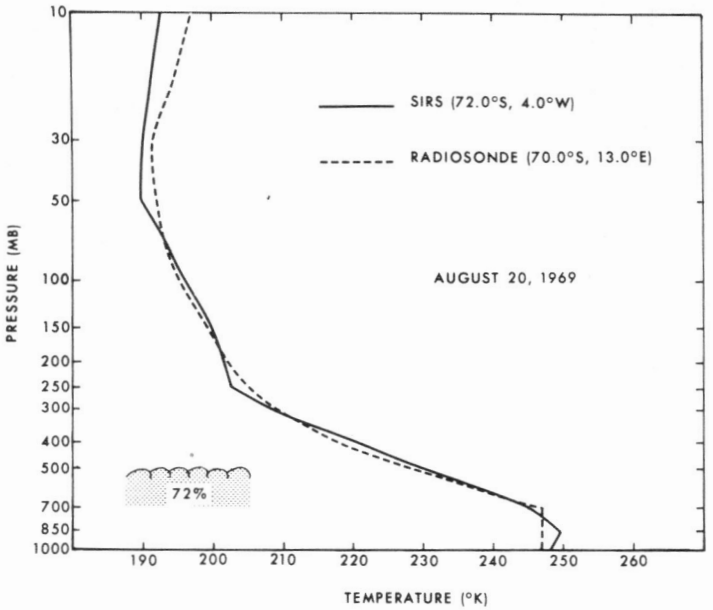

FIGURE 8.—Comparison of a SIRS-calculated and radiosonde-observed "Antarctic" temperature profile.

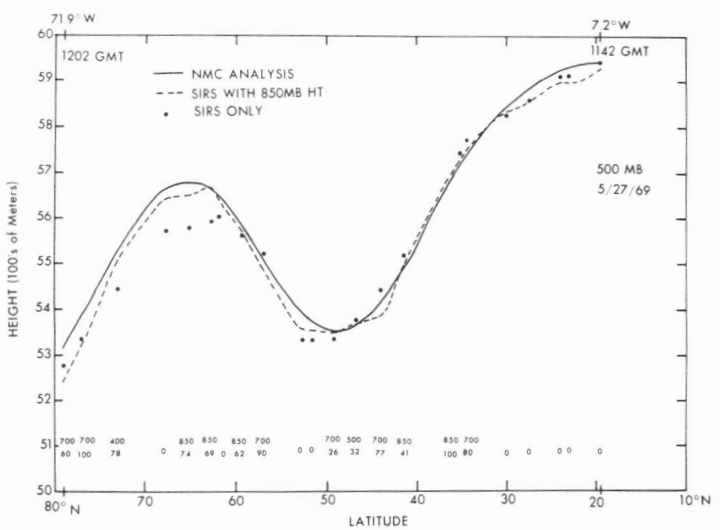

FIGURE 9.—Comparison of a latitude profile of 300-mb geopotential height obtained along an orbital track of Nimbus 3 from the SIRS and an analysis of conventional observations (denoted as NMC Analysis). The SIRS-calculated cloud pressures (in millibars) and cloud coverage (percent) are indicated below each SIRS sounding. A zero indicates a clear condition.

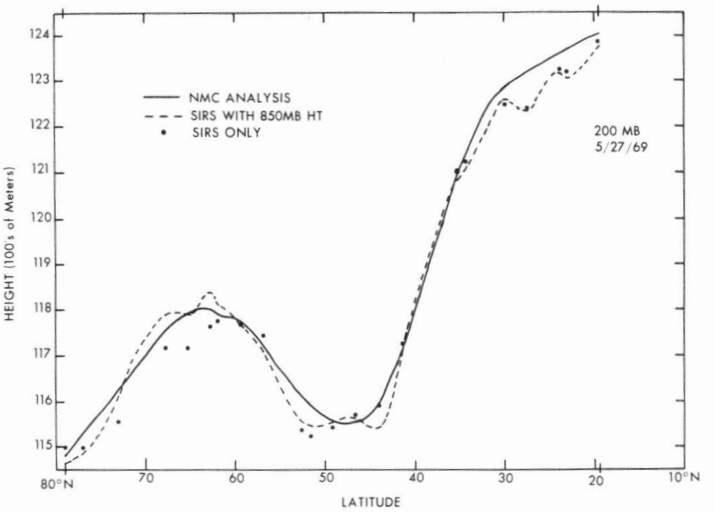

FIGURE 10.—Comparison of a latitude profile of 200-mb geopotential height obtained from the SIRS and an analysis of conventional observations.

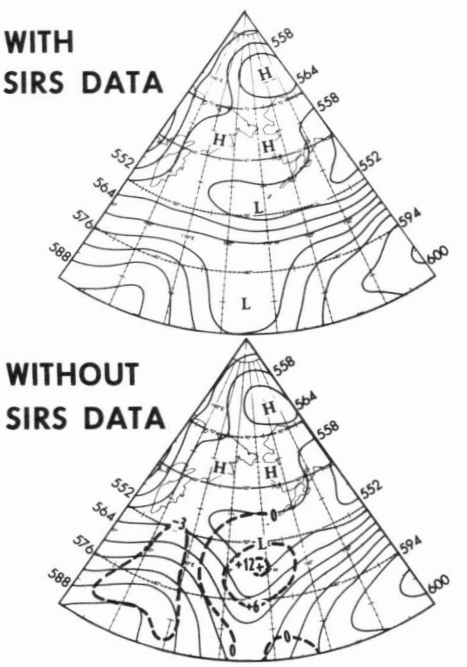

FIGURE 11.—Comparison of objective analyses of 500-mb height obtained with and without SIRS soundings. The differences in decameters are shown by the dashed isolines.

Accompanying the intensification of this trough is a short-wave ridge between it and the trough over the central United States. This feature is not noticeable in the forecast without the SIRS data.

Finally, figure 14 shows the differences in the two 3-day forecasts. The forecast for the United States based on the satellite analysis more closely resembles the observed situation. The trough near the west coast is now shown in the SIRS-based prognosis to be deeper than the one over the Great Plains, whereas the conventionally based prognosis showed only the single major trough over the Rockies and western Great Plains. The largest absolute errors of the SIRS forecast are only half the size of those of the prediction made without satellite data.

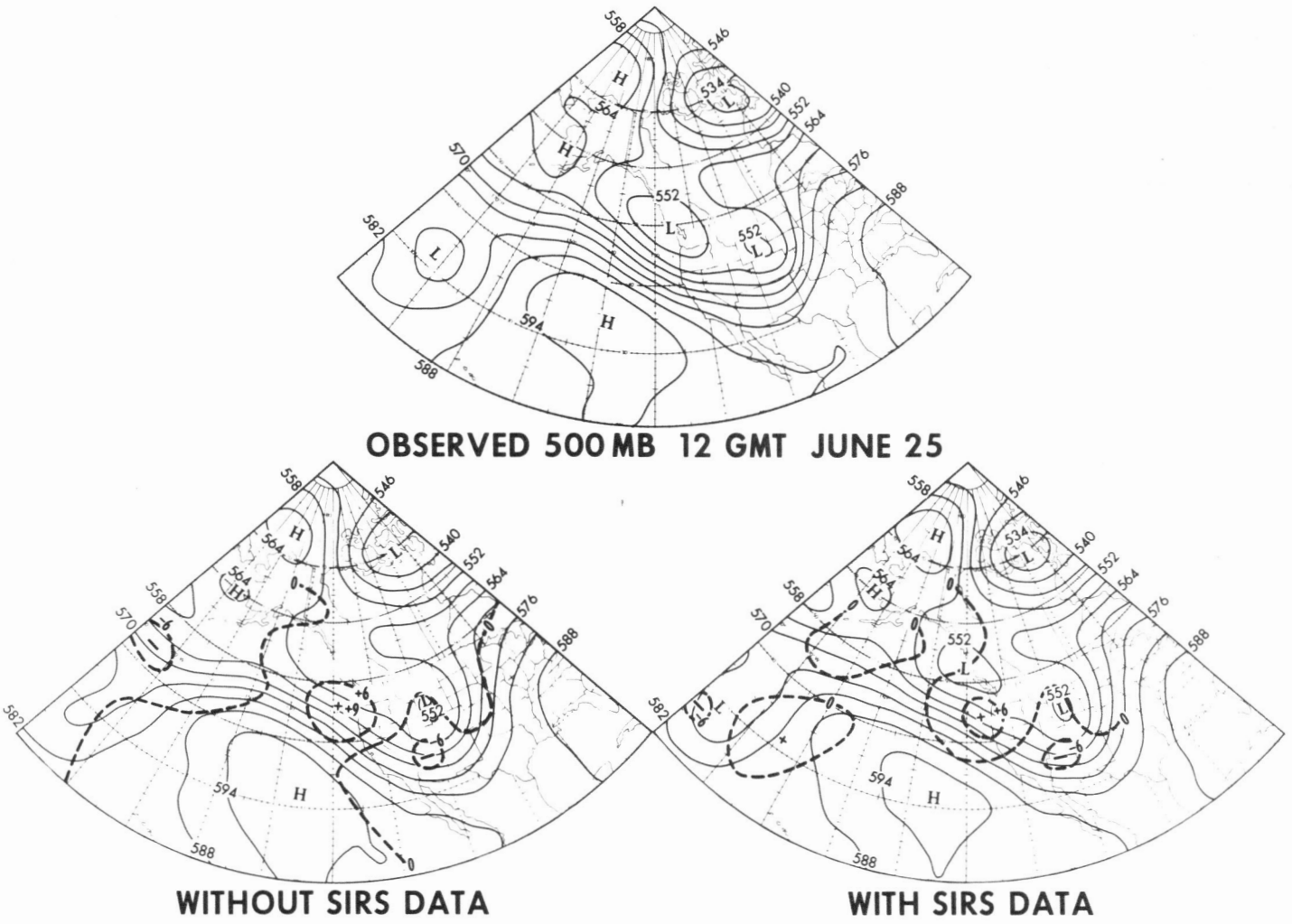

FIGURE 12.—Comparison of 24-hr primitive equation 500-mb forecasts obtained from the initial conditions specified with and without SIRS data. The differences of each forecast with the observed 500-mb distribution are indicated in decameters by the dashed isolines.

This example illustrates how a relatively small improvement in the analysis over the Pacific can produce a relatively large improvement downstream in a medium-range prediction. A few similar experimental comparisons have indicated only minor or no improvements in the forecasts. Differences in the initial conditions indicated by SIRS data are usually in the small-scale features in the middle latitudes of the Northern Hemisphere. Unfortunately it appears that current numerical analysis and forecast models do not respond sufficiently to small-scale differences in the initial conditions. Of course, part of the reason that the initial conditions are so similar is that SIRS data are included in the earlier analyses used to specify the "first guess" condition for the current analysis. In other words, in most of these forecast comparisons based on analyses with and without current SIRS data, the analysis without SIRS data has not been free of the influence of earlier SIRS soundings, especially in data-sparse areas.

Satellite spectral radiance measurements obtained from Nimbus 3 afford, for the first time, the opportunity to observe the temperature and mass distributions over vast areas of the Southern Hemisphere. As stated earlier, lack of surface temperature data, especially over continental areas where climatological estimates are inadequate, currently compromises the SIRS soundings of the troposphere. Additional complications in using the regression retrieval method in the Southern Hemisphere arise from the sparsity and biased distribution of the radiosonde observations.

Ten days of SIRS soundings obtained during a period of sudden stratospheric warming in August 1969 were used to construct daily analyses of constant pressure surfaces to determine how well the temperature and mass

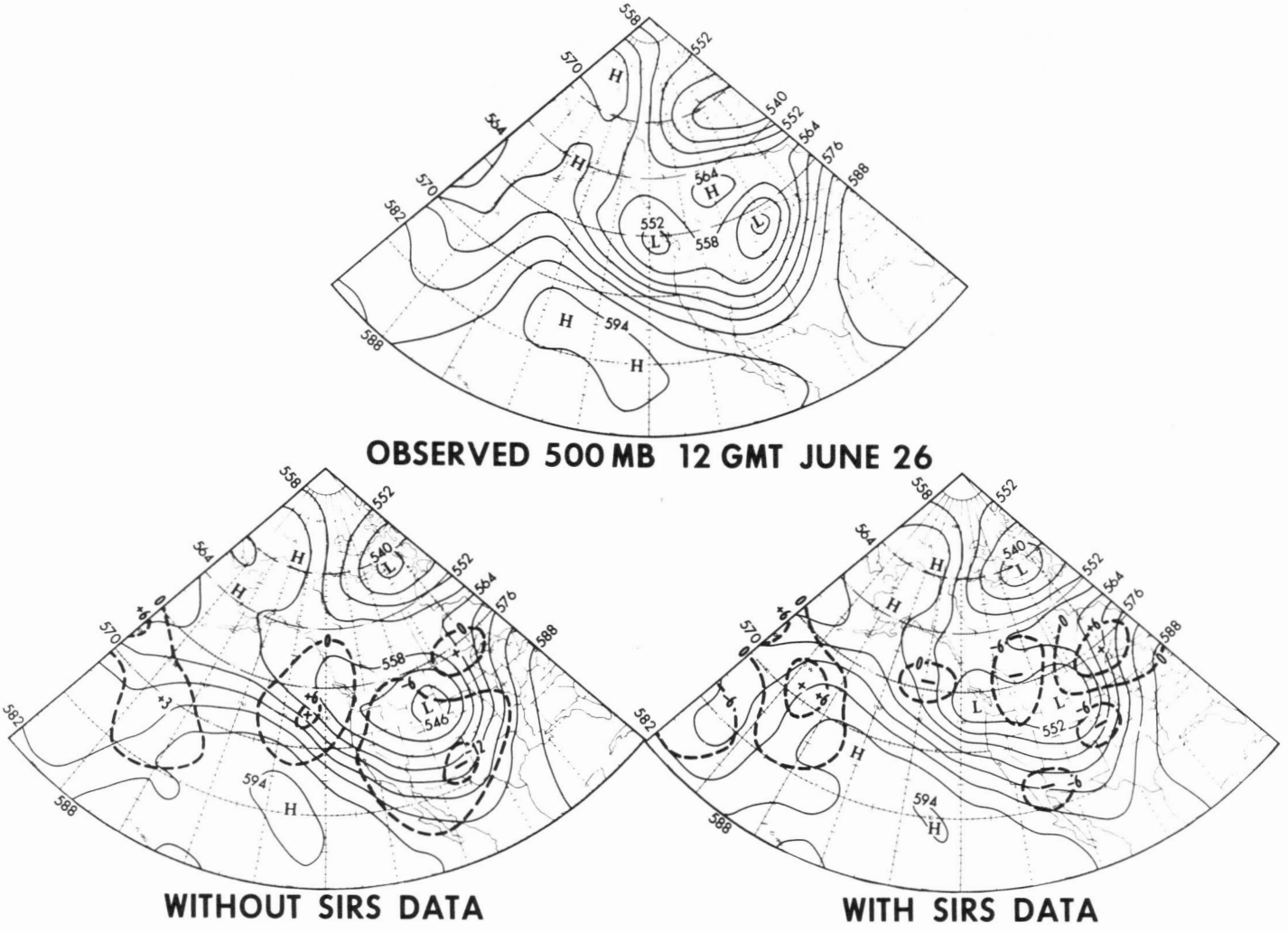

FIGURE 13.—Comparison of 48-hr 500-mb forecasts.

distribution of the Southern Hemisphere can be specified by regression from the SIRS observations. (The regression equations were derived mainly from July radiosonde and radiance data.) Each analysis was based on 24 hr of SIRS data (centered around 00 GMT) to provide complete hemispheric coverage. The analysis is most heavily weighted by the observations obtained near 00 GMT so that the resulting analysis would approximate a 00 GMT synoptic chart.

Figures 15, 16, 17, 18, and 19 show five of the temperature analyses obtained for the 30-mb level. This sequence of charts clearly illustrates the development and subsequent breakdown of a pronounced stratospheric warming. On August 14 (fig. 15), the thermal field is characterized by a circumpolar vortex with maximum temperatures at its periphery near −50°C. (Conventional radiosonde temperature observations (°C) are given on these charts to verify the accuracy of the SIRS-derived temperature analysis). There is a small area of slightly higher temperature centered near 47° S. and 50° E. On August 15 (fig. 16), the area of warm air has increased significantly and its center displaced to about 50° S. and 75° E. As shown, there were no conventional data to verify this warming trend. By August 16 (fig. 17), the temperatures at 30 mb have increased to values greater than −40°C. The warmest air is now located at 57° S. and 90° E. A few conventional radiosonde observations in this area verify the satellite-derived analysis. A maximum temperature of −22°C was observed over the same area at 10 mb with the SIRS measurements. Figures 18 and 19 show the subsequent breakdown of the warming. An interesting feature of the temperature distribution observed on August 19 is the beginning of a second warming on the western side of the hemisphere producing a bipolar temperature pattern.

Figure 20 shows a time-height cross section constructed from temperature profiles derived from SIRS observa-

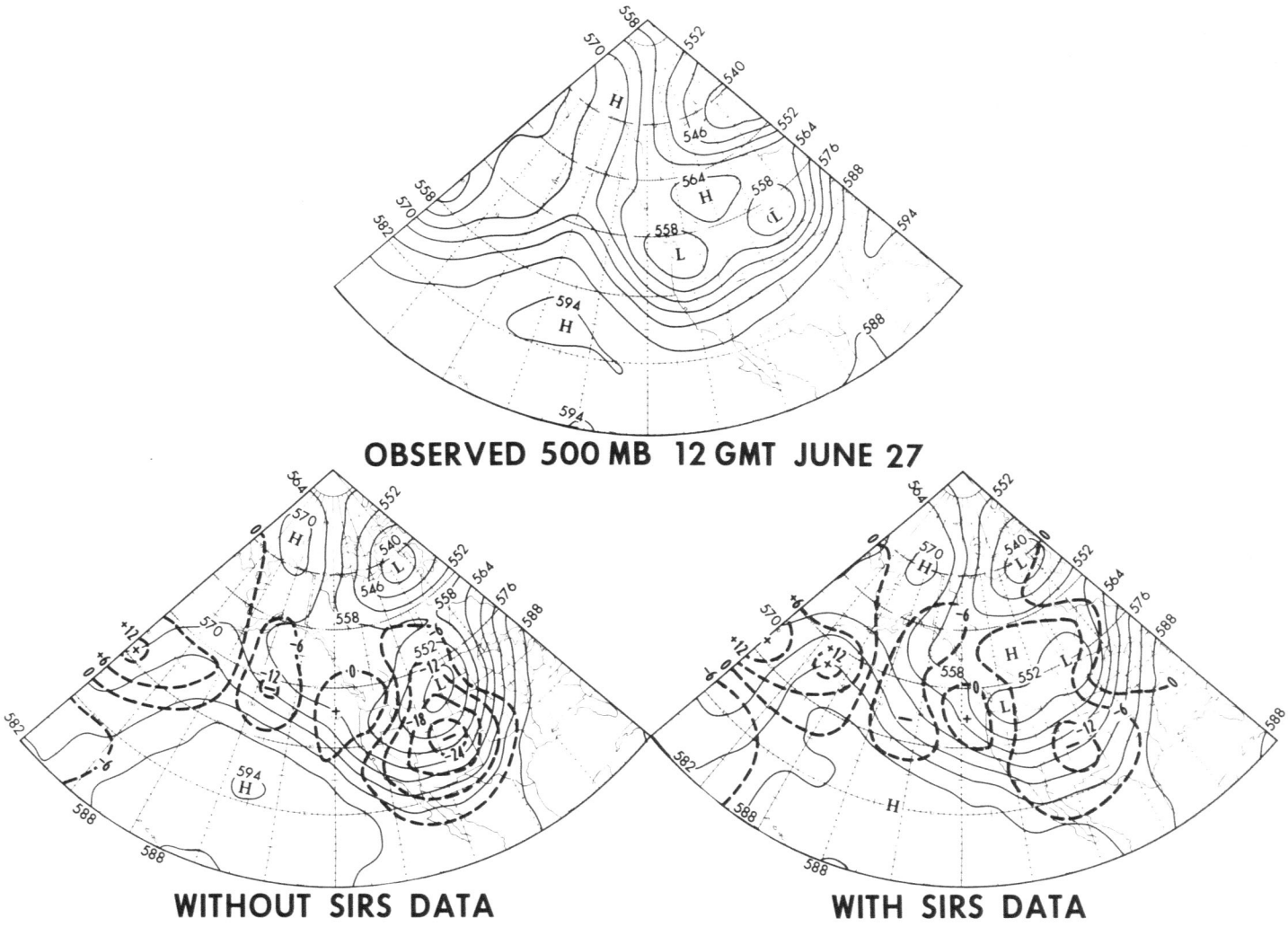

FIGURE 14.—Comparison of 72-hr 500-mb forecasts.

tions near the Mirny radiosonde station (66.5° S., 93° E.). The dramatic temperature changes observed in the SIRS data near the edge of the area where the sudden stratospheric warming occurred are verified quite well by Mirny radiosonde observations (the circled temperature values). All the results illustrate the ability of the SIRS instrument to detect, as well as the ability of the statistical method to retrieve, drastic stratospheric temperature changes.

Figures 21 and 22 show two examples of 300-mb geopotential height contour patterns derived solely from SIRS radiance observations. Available rawinsonde and aircraft wind reports are given for conventional verification. Considering the asynoptic character of the satellite data, the agreement of radiance-derived contour gradients with the conventional wind reports is felt to be good. The 24-hr movements of the major weather systems, shown by the heavy dashed arrows on figure 22, also appear to be quite reasonable. The only large discrepancies of SIRS-derived and radiosonde heights were noted over the Antarctic Continent. These discrepancies are probably due to the extremely high altitude of the surface.

The Southern Hemisphere results shown here are encouraging. The temperature and geopotential height determinations for the upper troposphere and stratosphere appear to be quite good. Major problems exist, however, in the middle and lower troposphere due to an inability to determine adequately the influence of clouds on the measured radiances. This deficiency is mainly due to the use of inaccurate surface temperature estimates. (Seasonal climatological normals have been used thus far in deriving soundings.) This problem should be alleviated when surface temperature observations are provided from the high resolution infrared window data soon to be obtained from the ITOS–1 satellite.

A pilot study has also been conducted to determine if satellite-derived temperature and geopotential height profiles may be useful in tropical analysis. Since only weak

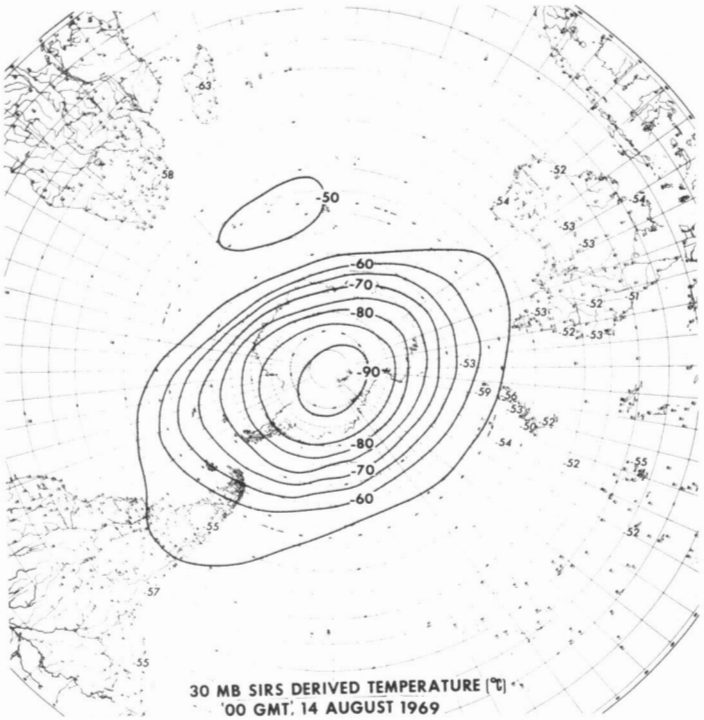

FIGURE 15.—Analysis of 300-mb temperature obtained from SIRS radiance observations. The analysis is based on 24 hr of satellite data centered around 00 GMT. The analysis is heavily weighted by the satellite observations obtained near 00 GMT to approximate a "00GMT" synoptic chart. The temperatures (°C) observed at 00 GMT by conventional radiosondes are given to verify the SIRS analysis.

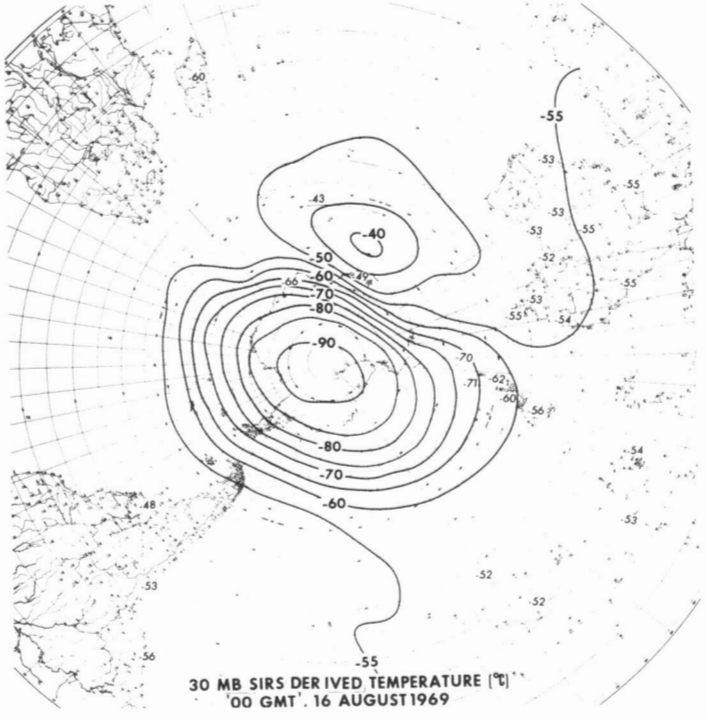

FIGURE 17.—Same as figure 15.

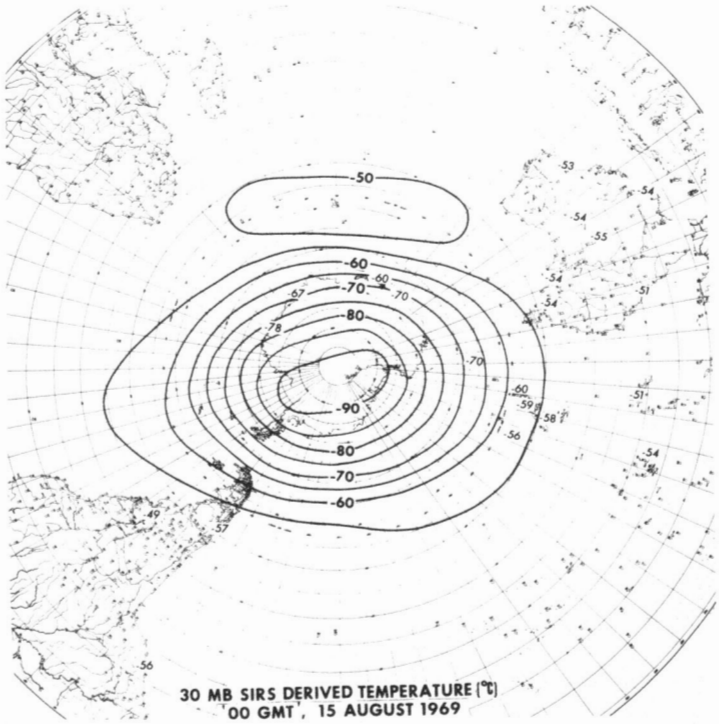

FIGURE 16.—Same as figure 15.

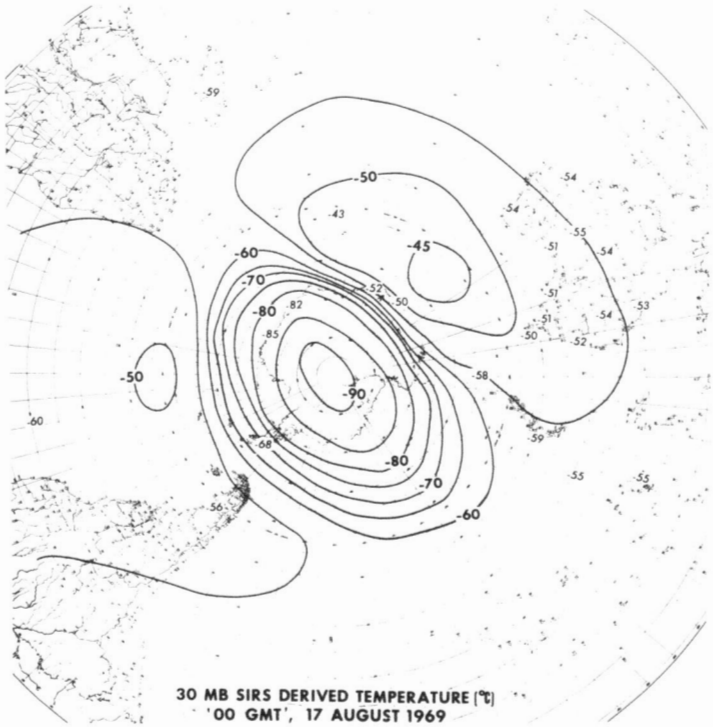

FIGURE 18.—Same as figure 15.

temperature and pressure gradients are required for significant atmospheric motions in tropical regions, temperature and pressure gradients must be specified to a very high degree of accuracy. In fact, conventional radiosonde accuracy is often marginal in tropical regions.

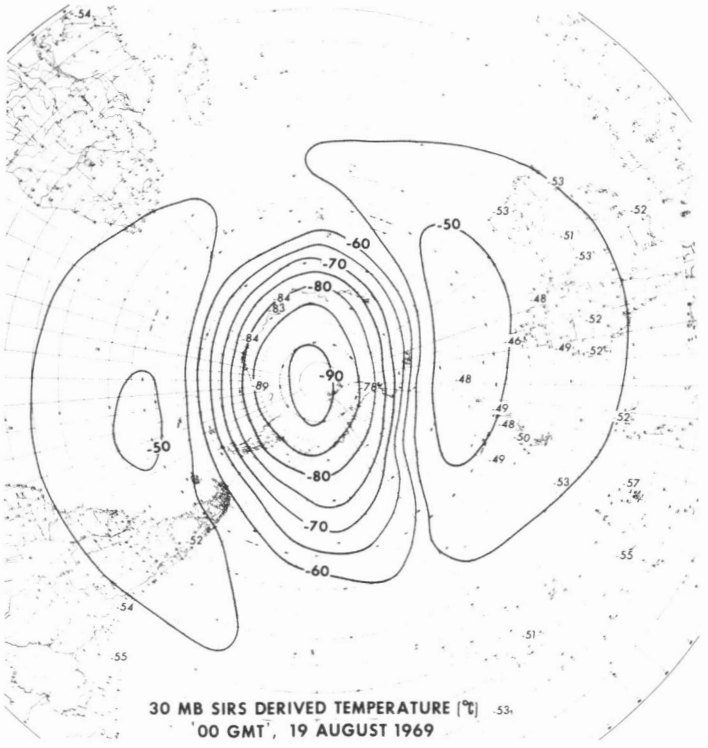

FIGURE 19.—Same as figure 15.

Thus, current analyses of tropical circulations depend very strongly on wind measurements.

There are large portions of the Tropics, however, devoid of wind observations. In such areas, satellite measurements of the temperature and pressure distribution, if sufficiently accurate, could be used to estimate the circulation patterns.

It is conceivable that temperature or pressure gradients can be measured more precisely from a single satellite than from pairs of conventional radiosondes. In the former case, instrumental bias errors will not significantly affect the accuracy of the derived gradient since the error will tend to cancel out. In the latter case, however, radiosonde errors will be random and therefore will not cancel out on the average when determining gradients.

Figure 23 shows two different tropical temperature distributions as measured by conventional radiosondes and observed by the SIRS. Major temperature differences between these two soundings, as large as 6°C, occur in the tropopause region. The SIRS soundings near these two radiosonde observations detect this difference at the tropopause very well. In the box on the right of figure 23, the brightness temperatures corresponding to the radiances for each channel at each location are shown. Note that the difference in the 692.3 cm^{-1} channel, the channel most sensitive to the tropopause region, was 0.8°C even though the retrieved soundings differ by 6°C. This occurs because the measured radiance in this channel eminates from a layer much larger than that in which these temperature differences exist. However, the profiles calculated from all the SIRS-measured radiances accurately describe the magnitude of the tropopause difference. This example not only illustrates the ability of the statistical inversion method to retrieve significant temperature differences in

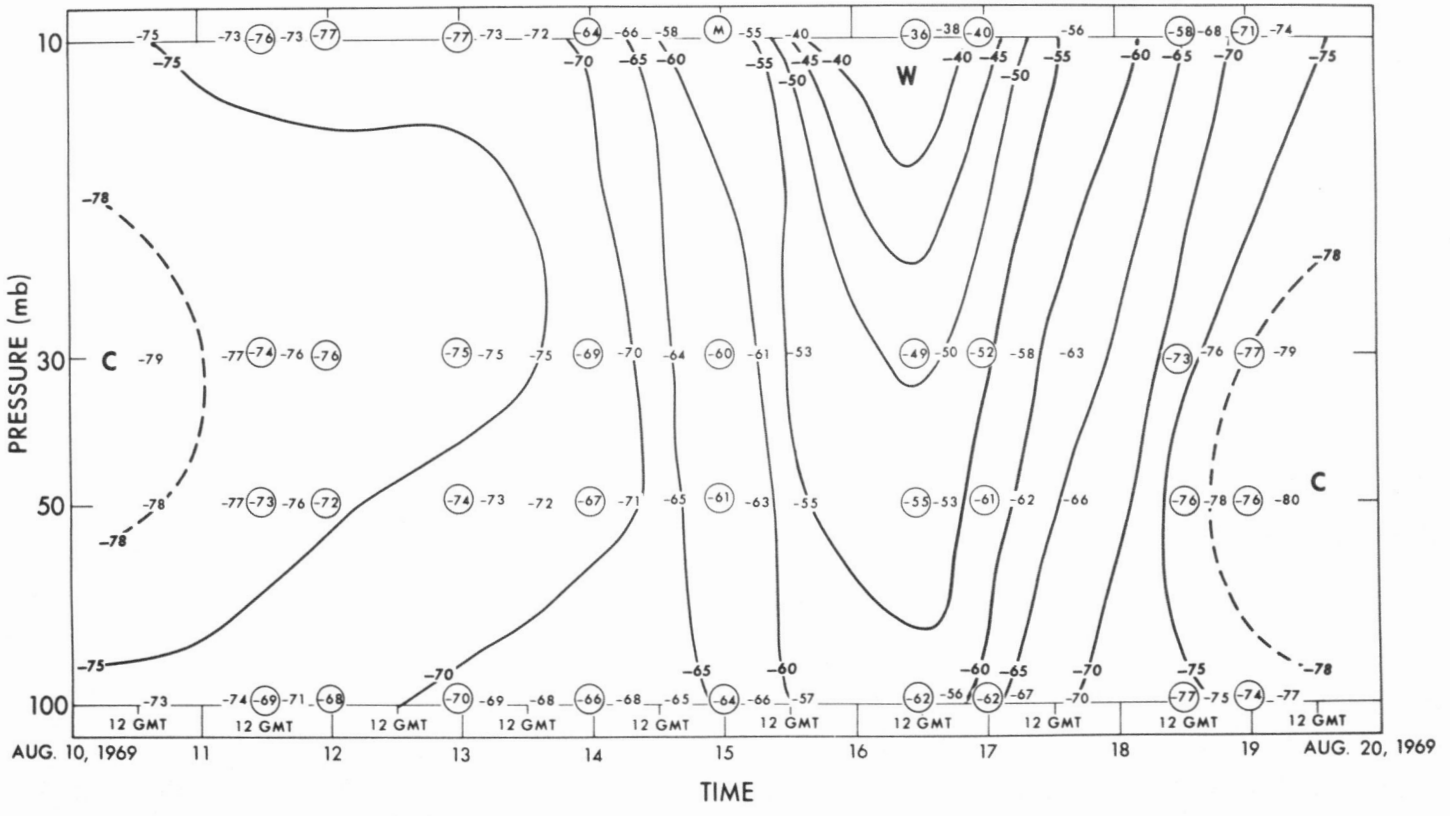

FIGURE 20.—Vertical time section of SIRS-derived temperature (°C) at 66.5° S. and 93° E. through the period Aug. 10, 1969, to Aug. 20, 1969. The analysis is based on the SIRS-derived temperatures (uncircled values). The temperatures reported by the Mirny radiosonde station (circled values) are given to verify the SIRS analysis.

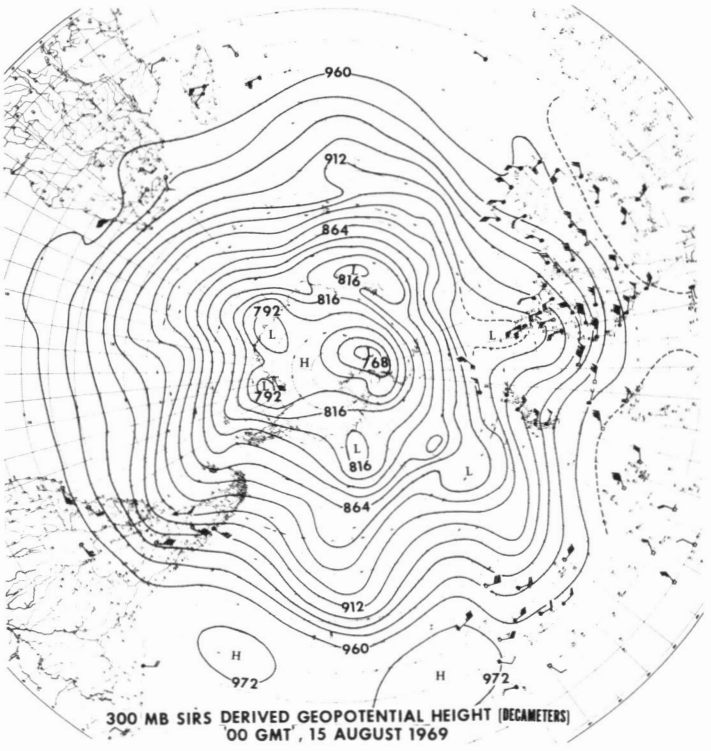

FIGURE 21.—Analysis of 300-mb geopotential height obtained from SIRS radiance observations. The analysis is based on 24 hr of satellite data centered around 00 GMT. The analysis is heavily weighted by the satellite observations obtained near 00 GMT to approximate a "00GMT" synoptic chart. Conventional rawinsonde observations obtained at 00 GMT (filled circles), at 12 GMT (open circles), and aircraft wind observations (squares) are given to verify the SIRS contour patterns.

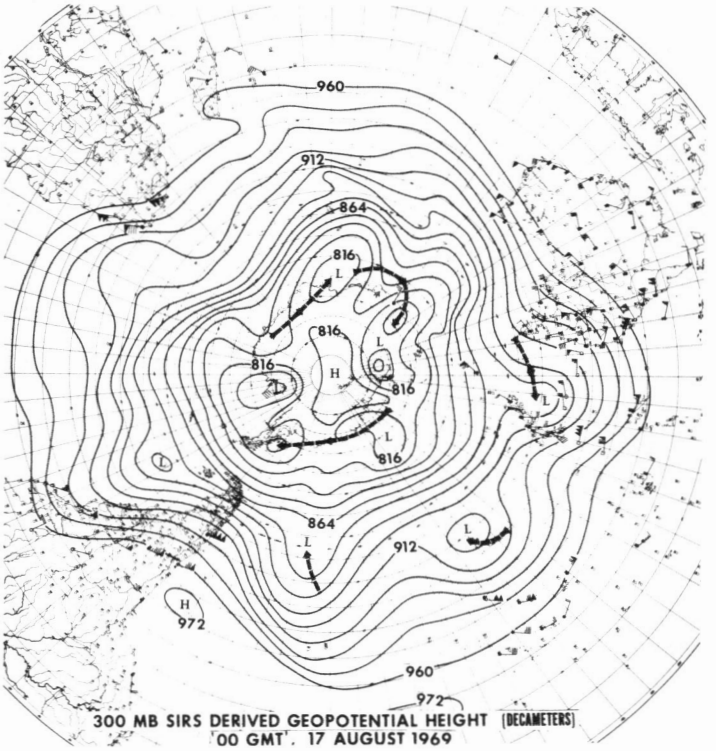

FIGURE 22.—Same as figure 21.

relatively shallow vertical layers but more important illustrates the precision of radiance measurements needed to detect such differences (that is, in this case, the difference of 0.8°C observed in the 692.3 cm^{-1} channel was associated with a 6°C tropopause temperature difference). Fortunately, the relative accuracy of the SIRS radiance measurements is better than 0.2°C.

SIRS-implied geostrophic winds were compared with those specified from conventional radiosonde, rawinsonde, and aircraft wind reports to determine how useful satellite-derived profiles might be in tropical analysis. The comparison was made with SIRS soundings obtained during the months between May and October of 1969. The geographical region considered was the Caribbean and Gulf of Mexico (15° N.–30° N., 70° W.–90° W.) owing to the large density of conventional observations.

Geostrophic wind components normal to the orbital tracks were computed from successive SIRS soundings through this region. The average distance between soundings is 3° of latitude. Comparative geostrophic winds implied by conventional data were obtained from the National Meteorological Center's operational isobaric contour analyses. The conventional analyses were initially interpolated to the satellite observation times.

Figure 24 shows a scatter diagram of the 300-mb geostrophic winds obtained from the conventional analyses and the geopotential heights statistically specified from SIRS radiances. The negative speeds denote easterly winds. The conventional analysis for 300 mb should be quite good because numerous aircraft wind reports are available for this level. The linear correlation coefficient of 0.71 seems quite significant considering the probable error of the conventional analyses. The standard error of 13.4 kt implies, at these latitudes, a standard error in the SIRS-specified geopotential height gradient of less than 5 m/degree-latitude or 15 m for the 3° spacing of soundings. The computed RMS error of the 300-mb height difference of adjacent SIRS soundings was about 20 m. These statistics imply that satellite-derived geopotential heights of adjacent soundings in the Tropics have a *relative accuracy* better than 10 m at 300 mb.

This result indicates that the gradients of temperature and geopotential height inferred from satellite observations might be sufficiently accurate to be useful in tropical analyses at least for latitudes greater than 15°. Incorporation of temperature and geopotential height gradients observed along orbital tracks into objective tropical analysis procedures should be very useful.

VERIFICATION STATISTICS

Figures 25, 26, and 27 show how well the SIRS-derived temperatures and geopotential heights compared with those obtained from objective analysis of radiosonde data.

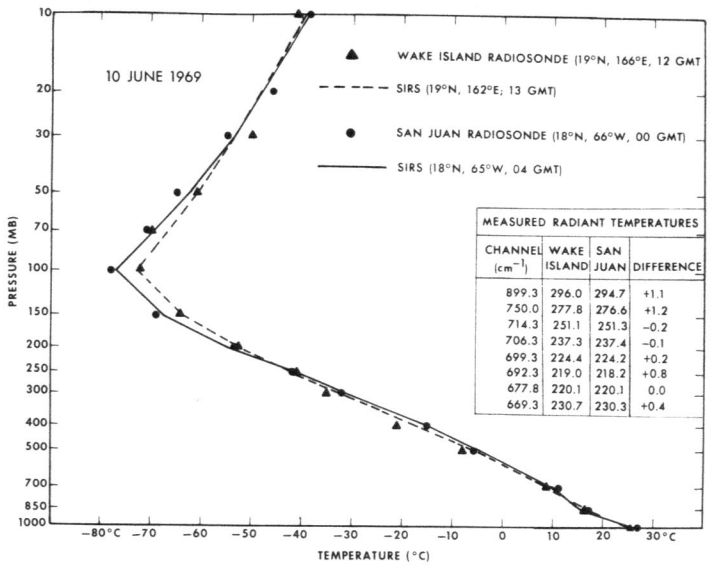

FIGURE 23.—Comparison of SIRS radiant (brightness) temperatures and derived soundings in the Tropics. Nearby radiosonde observations are shown to verify the SIRS retrievals.

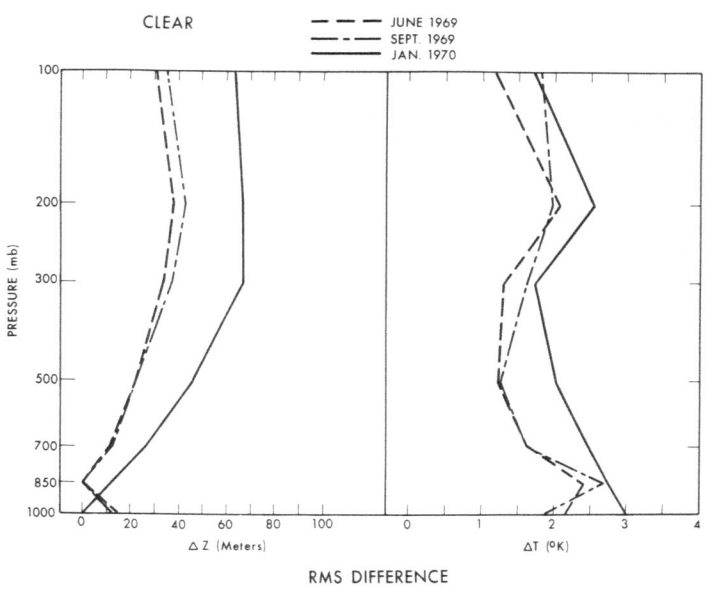

Figure 25.—Root-mean-square (RMS) difference between SIRS-derived and radiosonde-observed geopotential heights and temperatures for clear-sky conditions.

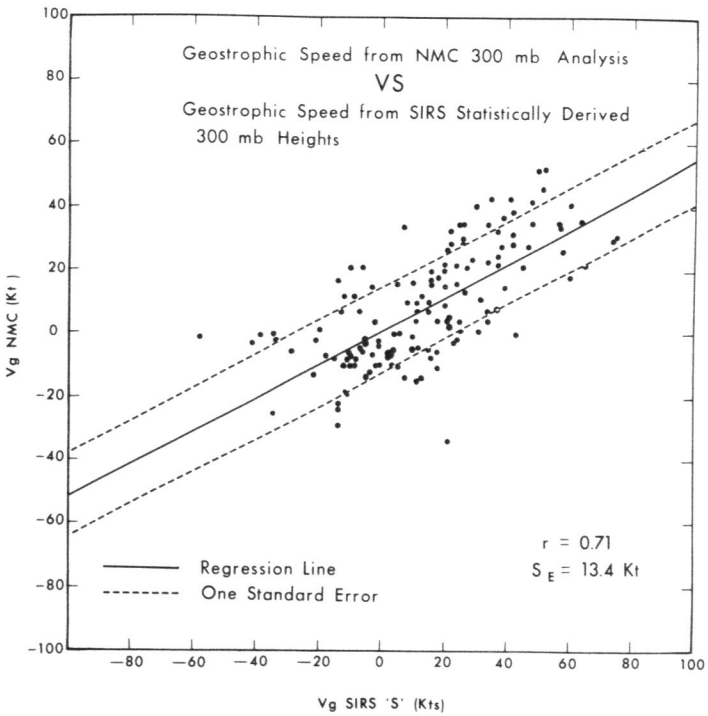

FIGURE 24.—Comparison of SIRS-implied 300-mb geostrophic winds and those deduced from conventional data obtained in the subtropics (15° N.–30° N., 70° W.–90° W.) May–October 1969.

These verification statistics were compiled from data over Western Europe (10° W.–60° E.; 40° N.–65° N.) where the SIRS radiances are observed within 3 hr of standard radiosonde release times (that is, 00 GMT and 12 GMT).

Figure 25 reveals the variation of the RMS differences between SIRS-derived and radiosonde-derived temperatures and heights with season for clear-sky conditions. As may be seen, the RMS differences were generally less than 30–40 m and 1.5°–2.0°C for the June and September samples. In January, the RMS geopotential height and temperature differences were nearly double these values. Part of the difference in the increase in geopotential height error (10–15 m) can be explained by the different reference heights used to correct the statistically specified heights (850 mb for June and September, 1000 mb for January). But most of the difference is due to the degradation of the SIRS temperature resolution *below* the 300-mb level. This is evident from the relatively large RMS temperature differences for January and the fact that the RMS height differences increase up to the 300-mb level. The constancy of the RMS height difference above 300 mb indicates that the mean temperatures of layers above 300 mb are in good agreement with radiosonde data, even though the temperatures of individual levels seem to show some random vertical discrepancies as indicated by the RMS temperature differences for January. The increase in the bias temperature errors below 300 mb, which led to increased height errors in the middle troposphere, is evidently due to the large noise level of the 714.3 cm^{-1} channel radiances that existed steadily after the early part of November. The 714.3 cm^{-1} channel is that channel most sensitive to the temperature in this region of the troposphere (fig. 2). The noise level of this channel was so excessive that it could no longer be used for calculations of temperature. As a result, the radiance-calculated temperatures in the troposphere became unreliable after the early part of November.

Figures 26 and 27 show RMS difference distributions for low and high cloudiness. (High cloud conditions were

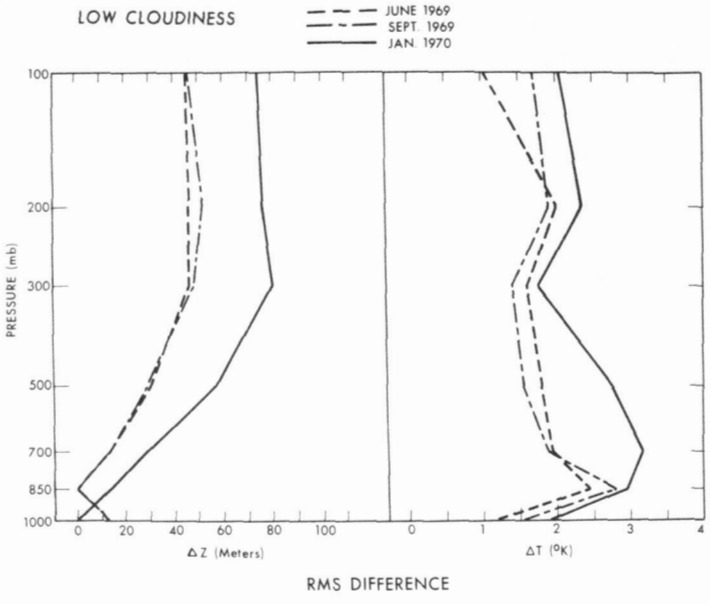

FIGURE 26.—RMS differences for low cloudiness conditions (that is, cloud obscuration less than 10 percent for cloud pressures less than 500 mb, less than 50 percent for cloud pressure equal to 500 mb, or less than or equal to 100 percent for cloud pressures greater than 500 mb).

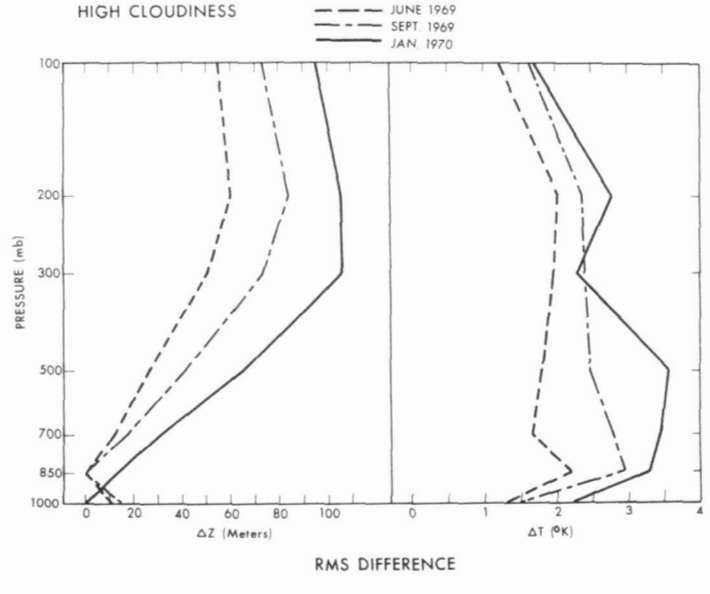

FIGURE 27.—RMS differences for high cloudiness conditions (that is, cloud obscuration greater than 10 percent for cloud pressures less than 500 mb or greater than 50 percent for cloud pressure equal to 500 mb).

classified as those in which the calculated cloud amount was greater than 50 percent for cloud pressures of 500 mb, or greater than 10 percent for cloud pressures less than 500 mb. All other cloud conditions were regarded as low cloudiness.) As expected, they reveal that the errors in radiance-calculated temperatures and geopotential heights worsen with increasing cloudiness. The relatively large discrepancies in January can also be attributed to the fact that the 714.3 cm^{-1} channel was excessively noisy during this month. Also, the correlation of middle tropospheric temperature with upper tropospheric and surface temperature most likely degrades as winter approaches. This latter consideration is most dramatically demonstrated in the high cloudiness condition where evidently a steady degradation of midtropospheric temperature accuracy occurs between summer and winter. This type of degradation does not occur for the clear and low cloudiness conditions (except that due to the loss of the 714.3 cm^{-1} channel), since in these situations the radiances are highly ensitive to the middle tropospheric temperature.

7. SUMMARY AND CONCLUSIONS

The SIRS experiment has demonstrated that meaningful vertical soundings can be obtained from satellites on a global scale. The first attempt to process the data on an operational basis made use of the statistical relations between radiosonde observations and the radiance observations as the interpretive algorithm. When all radiance channels were functioning properly, profiles with an accuracy comparable to that of radiosondes were obtained for clear-sky conditions. The accuracy of the temperatures in the troposphere and the heights at all levels are degraded by cloud obscuration, the degree of degradation being dependent on the amount and height of the clouds.

The accuracy of temperature and geopotential height profiles obtained from satellite radiometric measurements will improve significantly over the next few years. In the first place, high spatial-resolution scanning sounding radiometers, which are scheduled for flight in the latter part of 1971, will permit accurate temperature profiles to be calculated down to the earth's surface in all areas except those possessing an extensive overcast cloud condition (Smith 1969*a*, 1969*b*, 1969*c*). Second, improved statistical techniques, such as that used by Wark (1970), and nonstatistical techniques, such as that given by Smith (1970), will alleviate the dependence of the interpretive algorithm on current conventional data. With the implementation of these instrumental and data reduction improvements, it is anticipated that temperature and geopotential height profiles of radiosonde quality will be provided over most of the globe from satellite observations.

ACKNOWLEDGMENTS

We wish to thank Dr. D. Q. Wark and Mr. D. T. Hilleary, the developers of the SIRS experiment, for generously making their data available to us immediately after the initial measurements were obtained and continuously thereafter. We also wish to thank Mr. H. E. Fleming who has contributed significantly to the development of the retrieval technique. We wish to acknowledge the staff members of the National Environmental Satellite Center and the National Meteorological Center, who are too numerous to mention by name, for their contributions that have made the operational implementation of the SIRS data possible.

REFERENCES

Bradley, J. H. S., and Wiin-Nielsen, A., "On the Transient Part of the Atmospheric Planetary Waves," *Tellus*, Vol. 20, No. 3, **1968**, pp. 533–544.

Holmström, Ingemar, "On a Method for Parametric Representation of the State of the Atmosphere," *Tellus*, Vol. 15, No. 2, May **1963**, pp. 127–149.

Obukhov, A. M., "O statisticheski ortogonal'nykh razlozheniiakh empiricheskikh Funkstiĭ" (On Statistically Orthogonal Expansion of Empirical Functions), *Akademii Nauk SSSR, Izvestiia Seriia geofizicheskaia*, No. 3, Mar. **1960**, pp. 432–439.

Rodgers, C. D., "Satellite Infrared Radiometer; A Discussion of Inversion Methods," *University of Oxford Clarendon Laboratory Memorandum* No. **66.13**, England, **1966**, 25 pp.

Smith, William L., "A Polynomial Representation of Carbon Dioxide and Water Vapor Transmission," *ESSA Technical Report* NESC–47, U.S. Department of Commerce, National Environmental Satellite Center, Washington, D.C., Feb. **1969***a*, 20 pp.

Smith, William L., "Statistical Estimation of the Atmosphere's Geopotential Height Distribution From Satellite Radiation Measurements," *ESSA Technical Report* NESC–48, U.S. Department of Commerce, National Environmental Satellite Center, Washington, D.C., Feb. **1969***b*, 29 pp.

Smith, William L., "The Improvement of Clear Column Radiance Determination With a Supplementary 3.8μ Window Channel," *ESSA Technical Memorandum* NESCTM–16, U.S. Department of Commerce, National Environmental Satellite Center, Washington, D.C., July **1969***c*, 17 pp.

Smith, William L., "Iterative Solution of the Radiative Transfer Equation for Temperature and Absorbing Gas Profiles of an Atmosphere," *Applied Optics*, Vol. 9, No. 10, Oct. **1970** (to be published).

Smith, William L., and Fritz, S., "On the Statistical Relation Between Geopotential Height and Temperature-Pressure Profiles," *ESSA Technical Memorandum* NESCTM–18, U.S. Department of Commerce, National Environmental Satellite Center, Washington, D.C., Nov. **1969**, 16 pp.

Smith, William L., Rao, P. K., Koffler, R., and Curtis, W. R., "The Determination of Sea-Surface Temperature From Satellite High Resolution Infrared Window Radiation Measurements," *Monthly Weather Review*, Vol. 98, No. 8, Aug. **1970**, pp. 604–611.

Wark, D. Q., "SIRS, An Experiment to Measure the Free Air Temperature From a Satellite," *Journal of the Optical Society of America*, Vol. 60, **1970** (to be published).

Wark, D. Q., and Fleming, H. E., "Indirect Measurements of Atmospheric Temperature Profiles From Satellites: I. Introduction," *Monthly Weather Review*, Vol. 94, No. 6, June **1966**, pp. 351–362.

Wark, D. Q., and Hilleary, D. T., "Atmospheric Temperature: Successful Test of Remote Probing," *Science*, Vol. 165, No. 3899, Sept. 19, **1969**, pp. 1256–1258.

Westwater, Ed R., and Strand, Otto N., "Statistical Information Content of Radiation Measurements Used in Indirect Sensing," *Journal of the Atmospheric Sciences*, Vol. 25, No. 5, Sept. **1968**, pp. 750–758.

[*Received March 23, 1970; revised May 27, 1970*]